ANKARA YILDIRIM BEYAZIT UNİVERSITY

GRADUATE SCHOOL OF NATURAL AND APPLIED SCIENCE



FABRICATION AND CHARACTERIZATION OF ZnO: Ga/p-Si HETEROSTRUCTURE PHOTODIODES

M.Sc. Thesis by

Nur Efşan KÖKSAL

Department of Electrical and Electronics Engineering

January 2019

ANKARA

FABRICATION AND CHARACTERIZATION OF ZnO: Ga/p-Si HETEROSTRUCTURE PHOTODIODES

A Thesis Submitted to

The Graduate School of Natural and Applied Sciences of

Ankara Yıldırım Beyazıt University

In Partial Fulfillment of the Requirements for the degree of Master of Science

in Electrical and Electronics Engineering, Department of Electrical and Electronics Engineering

by

Nur Efşan KÖKSAL

January 2019

ANKARA

M.Sc. THESIS EXAMINATION RESULT FORM

We have read the thesis entitled **"FABRICATION AND CHARACTERIZATION OF ZnO: Ga/p-Si HETEROSTRUCTURE PHOTODIODES"** completed by **NUR EFŞAN KÖKSAL** under the supervision of **PROF. DR. ABDULLAH YILDIZ** and we certify that in our opinion it is fully adequate, in scope and in quality, as a thesis for the degree of Master of Science.

Prof. Dr. Abdullah YILDIZ

Supervisor

Prof. Dr. Sefer Bora LİŞESİVDİN

Jury Member

Assoc. Prof. Dr. Ahmet KARAARSLAN

Jury Member

Prof. Dr. Ergün. ERASLAN

Director

Graduate School of Natural and Applied Sciences

ETHICAL DECLARATION

I hereby declare that, in this thesis which has been prepared in accordance with the Thesis Writing Manual of Graduate School of Natural and Applied Sciences,

- All data, information and documents are obtained in the framework of academic and ethical rules,
- All information, documents and assessments are presented in accordance with scientific ethics and morals,
- All the materials that have been utilized are fully cited and referenced,
- No change has been made on the utilized materials,
- All the works presented are original,

and in any contrary case of above statements, I accept to renounce all my legal rights.

Date: 02.01.2019 **Signature: ……..**

Name &Surname: Nur Efşan KÖKSAL

ACKNOWLEDGEMENTS

I would like to sincerely thank my supervisor, Prof. Dr. Abdullah YILDIZ for his great support and encouragement during my M.Sc. studies. He always shared his knowledge and experience with me.

I would like to also thank all my colleagues in the laboratory, especially Mohamed SBETA, Aycan ATLI and Abdullah ATILGAN, for their support, advice and help during my thesis work.

I owe my most sincere gratitude to my dear family, who are always with me and provided full support during my hard studies. Also, I would like to especially thank my lovely nephew, Kutay KÖKSAL, because he always loves me as his aunt, and this made me stronger during my hard studies.

2019, 2 January **Nur Efşan KÖKSAL**

FABRICATION AND CHARACTERIZATION OF ZnO: Ga/p-Si HETEROSTRUCTURE PHOTODIODES

ABSTRACT

The Ga-doped ZnO (GZO)/p-Si photodiodes with different thicknesses of the GZO layer were fabricated using a sol-gel method. Thin film properties were determined by means of X-Ray Diffraction, Atomic Force Microscopy, and UV-VIS spectrophotometer measurements. The average grain size, texture coefficient, RMS value and transparency of GZO films were estimated. The current-voltage characteristics of the devices were measured in the dark and under AM1.5 illumination to investigate photoelectrical properties of the devices. Some important parameters such as saturation current, ideality factors and barrier heights were obtained. The rectification ratio, photosensitivity and responsivity values were improved with presence of thinner GZO layer.

The results indicate that the device with thinner GZO layer exhibited the highest performance in terms of photodiode. We reached the better device performance than those reported in the literature over AM1.5 illumination.

Keywords: Ga-doped ZnO thin films, photodiode and sol-gel

ZnO: Ga/p-Si HETEROYAPI FOTODİYOTLARIN ÜRETİMİ VE KARAKTERİZASYONU

ÖZ

GZO tabakasının farklı kalınlıklarına sahip olan Ga-katkılı (GZO)/Si fotodiyotlar sol-gel yöntemi kullanılarak üretildi. İnce film özellikleri, XRD, AFM ve UV-VIS spekrometre ölçümleri yardımıyla belirlendi. GZO filmlerin ortalama tanecik büyüklüğü, doku katsayısı, RMS değeri ve transparanlığı hesaplandı. Cihazların akım-gerilim karakteristikleri, fotoelektriksel özelliklerini incelemek için AM1.5 ışığı altında ve karanlıkta ölçüldü. Doyma akımı, idealite faktörü, bariyer yüksekliği gibi bazı önemli parametreler elde edildi. Doğrultma oranı, ışığaduyarlılık ve duyarlılık değerleri daha ince GZO tabakasının varlığıyla geliştirildi.

Sonuçlar, daha ince GZO tabakasına sahip cihazın fotodiyot açısından en iyi performansı gösterdiğini belirtti. Literatürde bildirilenlere kıyasla en iyi cihaz performansına AM1.5 aydınlatmasında ulaştık.

Anahtar kelimeler: Fotodiyot, Ga-katkılı ZnO ince filmler ve sol-gel

CONTENTS

M.Sc. THESIS EXAMINATION RESULT FORM ii
ETHICAL DECLARATION iii
ACKNOWLEDGEMENTS iv
ABSTRACT v
ÖZ vi
NOMANCLATURE ix
LIST OF TABLES xii
LIST OF FIGURES xiii

CHAPTER 1- INTRODUCTION 1
1.1 Properties of Zinc Oxide 1
1.2 Doping 2
1.3 The p-n Junction Diodes 3
1.4 Photodiodes 8
1.5 Fundamental Working Principles of Photodiodes 8
1.6 Equivalent Circuit 9
1.6 The Applications of Photodiodes 11
1.7 Literature Review 11
CHAPTER 2- DEVICE FABRICATION 14
2.1 The solution preparation for ZnO: Ga 15
2.2 Cleaning Process for Si Substrates 16
2.3 Deposition 18
2.4 Metallization 19
CHAPTER 3- DEVICE CHARACTERIZATION 21
3.1 X-Ray Diffraction Measurements 21
3.2 Atomic Force Microscopy Measurements 22
3.3 The Scanning Electron Microscopy Measurements 23
3.4 UV-VIS-NIR Measurements 24
3.5 Current-Voltage Measurements 25
CHAPTER 4- RESULTS AND DISCUSSIONS 26
4.1 X-Ray Diffraction Results 26
4.2 Atomic Force Microscopy Results 29

4.3 Scanning Electron Microscopy Results 31
4.4 UV-VIS-NIR Results 34
4.5 The Current-Voltage Results..... 37
CHAPTER 5- CONCLUSION..... 45
REFERENCES..... 48
CURRICULUM VITAE..... 56

NOMANCLATURE

Symbols

β	Full-width at half-maximum
C_j	Junction capacitance
d	Interplanar spacing
E_{field}	The internal electrical field
I_{sc}	Short-circuit current
I'	Shunt resistance current
I_L	Photocurrent
I_D	Diode current
I_{dark}	Dark current
I_o	Output current
I_{ph}	Photo-generation current
M	Molarity
P_{in}	Input power
R_S	Series resistance
R_{sh}	Shunt resistance
V_A	Applied voltage
V_D	Diode voltage
V_o	Output current
V_{oc}	Open circuit voltage
λ	Wavelength
2θ	Measured between the incident beams called as Bragg angle
Ω	Ohm

Acronyms

AFM	Atomic Force Microscopy
Al	Aluminum
Ag	Silver
Au	Gold
Au	Arbitrary unit
B	Boron

BGZO	Boron Gallium ZnO
CVD	Chemical vapour deposition
D	Average grain size
EtOH	Ethanol
Ga	Gallium
GaN	Gallium nitrate
Ga (NO_3)	Gallium nitrate hydrate
GZO	Gallium doped zinc oxide
HF	Hydrofluoric acid
In	Indium
K	Potassium
LD	Laser diodes
LEDs	Light emitting diodes
MEA	Monoethanolamine
N	Nitrogen
Na	sodium
NWs	Nanowires
P	Phosphorous
Pb	Lead
R	Responsivity
PS	Photosensivity
RR	Rectification ratio
Si	Silicon
SiO_2	Silicon dioxide
Sn	Tin
nm	Nanometer
ml	Mililiter
T_{avg}	Average transmittance
TC	Texture coefficient
Ti	Titanium
TFT	Thin film transistors
UV	Ultra violet
V_B	The barrier height
V_{bi}	The built-in voltage

XRD	X-ray Diffraction
ZAD	Zinc acetate dihydrate
ZnO	Zinc oxide
2D	Two dimension
3D	Three dimension

LIST OF TABLES

Table 2.1 The quantities used for the chemical solution 15

Table 4.1 List of 2θ, β, D for Ga-doped ZnO thin films for different coating cycles 27

Table 4.2 List of c, d, and ε for Ga-doped ZnO thin films according to coating cycles 29

Table 4.3 List of RMS values 31

Table 4.4 The variation of particle size with thickness 33

Table 4.5 List of average transmittances 36

Table 4.6 List of band gaps 37

Table 4.7 List of I_s, n, $\emptyset_b$ and PS, RR and R 42

Table 4.8 The comparison of PS, RR and R for ZnO/Si with the previous works 43

LIST OF FIGURES

Figure 1.1 Schematic structure of hexagonal wurtzite crystal structure of ZnO [10]. 1

Figure 1.2 Fundamental structure of the p-n junction diode with space charge region 3

Figure 1.3 The p-n junction diode under thermal equilibrium [35] 4

Figure 1.4 The p-n junction diode under forward bias [38] 6

Figure 1.5 The p-n junction diode under reverse bias [38] 7

Figure 1.6 Equivalent circuit of a photodiode [42] 9

Figure 1.7 The current-voltage characteristics of a photodiode with Voc and Isc [43] 10

Figure 2.1 The fundamental structure of the photodiode 14

Figure 2.2 The n-type GZO solution preparation process 16

Figure 2.3 The cleaning process for Si wafers 17

Figure 2.4 The picture of the spin coater used for preparing thin films 18

Figure 2.5 The picture of GZO thin film on p-silicon after the deposition process .. 19

Figure 2.6 The rear silver contact (left) and the top silver contacts (right) 19

Figure 2.7 After the metallization, silicon substrates with different thicknesses 19

Figure 3.1 XRD measurement device (Rigaku Miniflex 600 Table) 21

Figure 3.2 AFM measurement device (Quesant Ambious Q-scope series) 22

Figure 3.3 SEM measurement device (QUANTA 400F Field Emission SEM) 23

Figure 3.4 The UV-VIS-NIR Shimadzu Corporation UV-1700 24

Figure 3.5 The Keithley 2400 SMU I-V measurement device with solar simulator 25

Figure 4.1 XRD results of Ga-doped ZnO thin films for different coating cycles ... 26

Figure 4.2 The 2-D (left) and 3-D (right) AFM images a) 1-cycle b) 3-cycle c) 5-cycle 30

Figure 4.3 The top view of the SEM micrographs a) 1-cycle b) 3-cycle and c) 5-cycle 32

Figure 4.4 The cross-sectional view of the SEM micrographs for 5-cycle 33

Figure 4.5 Transmittance spectra of ZnO thin films with various coating cycles 34

Figure 4.6 Absorbance spectra of Ga-doped thin films for different coating cycles 36

Figure 4.7 The $(\alpha h\nu)2$ versus photon energy for GZO thin films on glass substrates 37

Figure 4.8 Current-voltage curve for n-GZO/p-Si photodiodes under dark conditions 41

Figure 4.9 Current-voltage curve for GZO/p-Si photodiodes under light condition 42

Figure 4.10 The semilog I-V graph with different thicknesses under light and in the dark..... 44

CHAPTER 1

INTRODUCTION

This section provides some information on ZnO, doping of ZnO, p-n junction diodes, photodiodes, fundamental working principles of photodiodes and equivalent circuit, as well as a literature review.

1.1 Properties of Zinc Oxide

A II-VI semiconducting compound, ZnO has been studied on for many years. ZnO has a direct wide band gap (~3.3 eV) and possesses large exciton binding energy (~60 meV) at 300 K, large carrier mobility (> 100 $cm^2/V.s$), high transparency with low resistivity properties and good electrical conductivity [1-4]. ZnO is an inexpensive non-toxic material, presents in large quantities in nature and provides a convenience of doping [5-9].

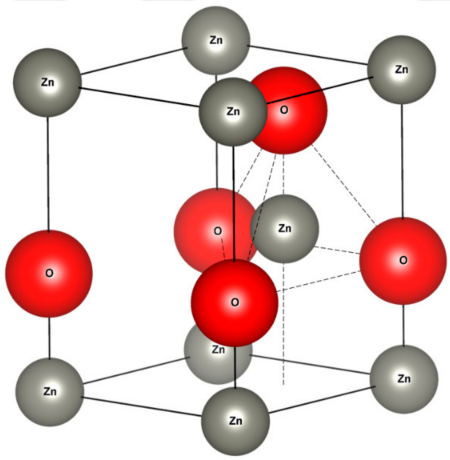


Figure 1.1 Schematic structure of hexagonal wurtzite crystal structure of ZnO [10]

Hexagonal wurtzite crystal structure of ZnO is given in Figure 1.1. In this structure, the ratio (*a/c*) of the *a* and *c* values, which are the lattice parameters, is about 1.6 [10].

ZnO has been utilized to fabricate electronics devices, such as panel displays [11], light emitting diodes (LEDs) [12], thin film transistors (TFTs) [13], laser diodes (LD) [14], solar cells [15], gas sensors [16] and photodiodes [17]. The atomic layer deposition [18], chemical vapor deposition (CVD) [19], sputtering [20], spray pyrolysis [21] and sol-gel [1] are commonly used methods for ZnO layer deposition.

Due to the superior properties of ZnO, in this study, ZnO was selected to fabricate a photodiode with better properties than those in previous literature.

1.2 Doping

ZnO is not only synthesized as undoped but can also be doped with some elements. Pure ZnO is a compound that tends to oxidize because of its high oxygen absorption. The high temperature (above 700℃) needed to obtain ZnO creates defects like vacancy and interstitials in the ZnO. The greater oxygen absorption and defects affect poorly the electrical conductivity of ZnO. Therefore, doping with different elements aims to improve the electrical conductivity and reduces the defects in the ZnO [22-24].

ZnO exhibits the properties of either n-type or p-type semiconductors as a result of doping. The methods, used to obtain the p-type compound have not yet been sufficiently developed. In the p-type doping process for obtaining the ZnO compound, group-I or group-V elements, such as sodium (Na), potassium (K), nitrogen (N), and phosphorus (P) in the periodic table, are used as doping materials. To make ZnO semiconductors n-type, ZnO is doped with group-III elements, such as gallium (Ga), aluminum (Al), indium (In) and boron (B), or group-IV elements, such as tin (Sn) or lead (Pb). Thus, the electrical, optical, structural, chemical and morphological properties of ZnO can be enhanced [2, 25, 26].

Due to some superior properties of Ga over other dopants, Ga is the desired dopant atom for ZnO. The covalent bond length and ionic size of dopants are important parameters for doping. The ionic radius of Ga^{+3} is 0.062 nm and Zn^{+2} is 0.074 nm, and the covalent bond length of Ga-O is 0.192 nm and Zn-O is 0.197 nm. Because the ionic radius of Ga^{+3} and the covalent bond length of Ga-O are slightly lower than

Zn^{+2} and Zn-O, respectively, Ga can easily substitute location of Zn with low lattice imperfections even at high Ga concentrations [27-30].

Furthermore, Ga-doped thin films (GZO) have many additive advantages. They have high transparency (above 85%) in the visible range (between 400 and 800 nm wavelengths), strong resistances against oxidation and high chemical stability. They are non-toxicity and have excellent sensitivity to UV light, so GZO is quite suitable as a dopant. Also, Ga can be used in photodiode devices [3, 25, 30-32].

Finally, Ga was selected as a dopant, in this study, because of its having excellent properties as mentioned before.

1.3 The p-n Junction Diodes

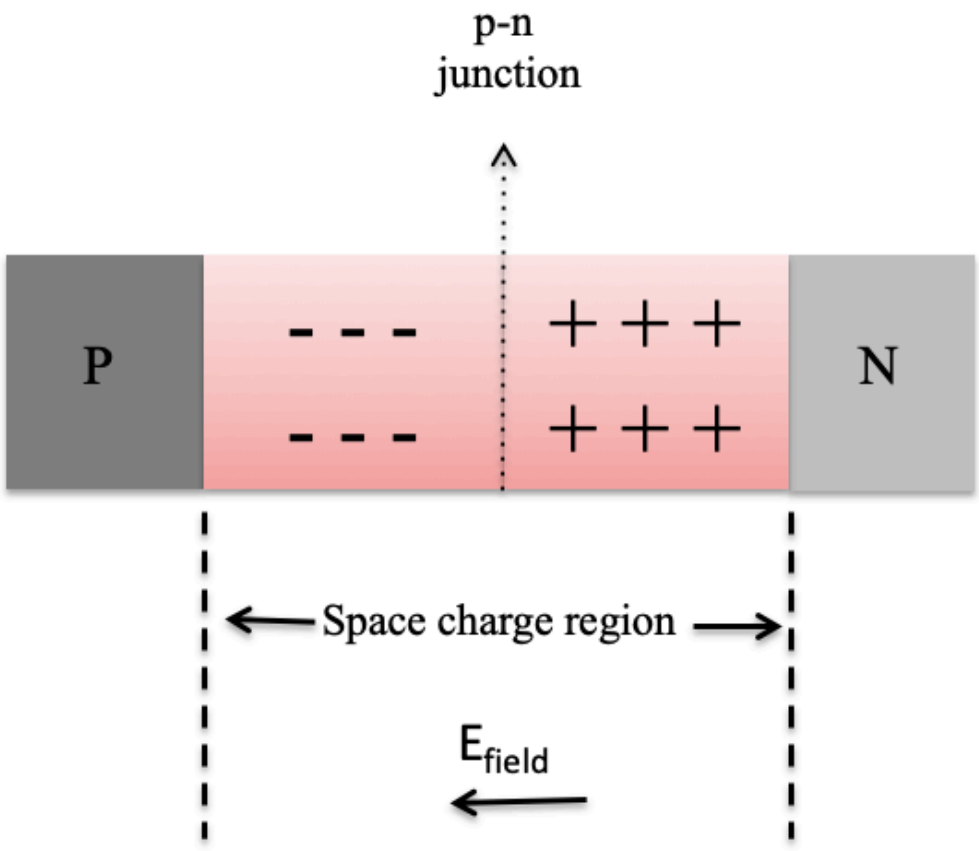


Figure 1.2 Fundamental structure of the p-n junction diode with space charge region

The working principles of many electronic devices, such as solar cells, lasers, LEDs, transistors and photodiodes, are based on the p-n junction diodes. The *p-n junction* is an interface between the p-type and n-type regions in the semiconductors. While the holes are majority carriers in the p-type semiconductor and electrons are majority carriers in the n-type region, the holes are minority carriers in the n-type semiconductor and the electrons are minority carriers in the p-type semiconductor. A junction of n-type and p-type semiconductors causes a diffusion current of electrons from n-type to p-type and a diffusion current of holes from the p-type region into the n-type region. The electrons moved from the n-type region to the p-region combine with holes in the region that is near the junction. The atoms that lose their electrons in the n-region are positively charged, while the atoms that accept electrons in the p-region are negatively charged. In this way, a region called *space charge region (depletion region)* occurs where positive ions are on the n-type region and negative ions are on the p-type region. This is schematically illustrated in Figure 1.2 [33, 34].

1.1.1 The p-n Junction Diodes Under Thermal Equilibrium (Zero Bias)

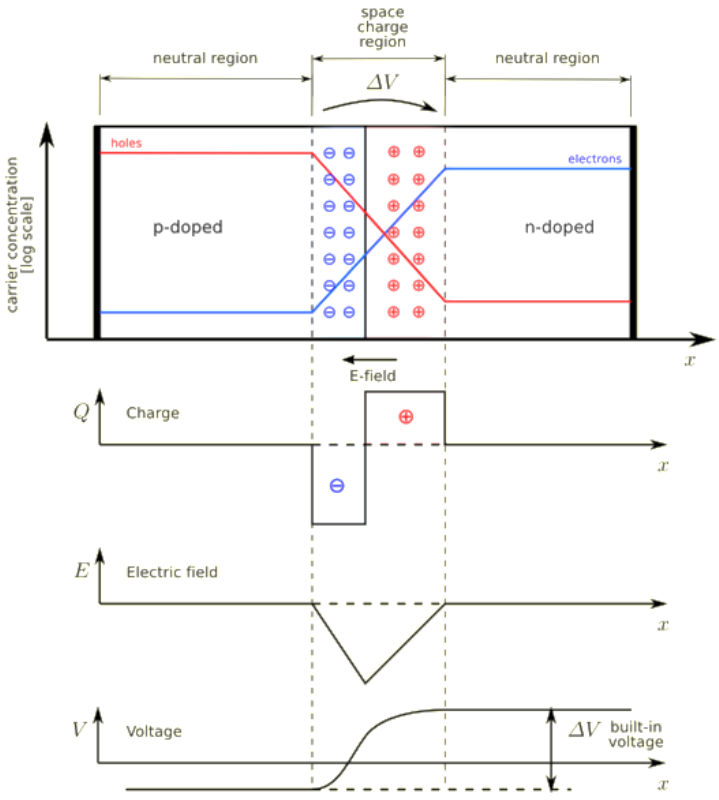


Figure 1.3 The p-n junction diode under thermal equilibrium [35]

When any external input, such as voltage or light, is not applied to a p-n junction, it is called a p-n junction in thermal equilibrium conditions (presented in Figure 1.3). The internal electric field (E_{field}) with a direction from n-type to p-type is comprised between p and n type regions. An electric field in this region causes a potential difference because there is a change in the energy level. This electric field prevents more carriers from crossing the junction and forms a barrier voltage (V_B) or built-in potential (V_{bi}) in the depletion region. This internal electric field forces the charge carriers to move in the opposite direction. Any net current does not flow across the p-n junction since the diffusion force and the E_{field} completely stabilize one another, which is called *thermal equilibrium with zero bias*. The Fermi level, which is an average energy level of electrons, has a constant position under equilibrium. In the out of space charge region, the valence and conduction bands do not exhibit any change to the Fermi level and the concentration of charge carriers. The concentration of charge carriers suddenly reduces in the space charge region. When a diode is in the thermal equilibrium with zero bias, the built-in potential is roughly 0.6 V to 0.7 V in the silicon semiconductor diodes, whereas built-in potential is approximately 0.3 V in the germanium semiconductor diodes [33, 36, 37].

1.1.2 The p-n Junction Under Forward Bias

When a p-n junction diode is under a forward bias condition, a p-type semiconductor is linked with a positive voltage terminal and an n-type semiconductor is connected to a negative voltage terminal (displayed in Figure 1.4). Electrons in the n-region and holes in the p-region are repelled to the junction in order to pass over the junction and integrate with the opposite charges. The applied forward voltage will diminish the potential difference. The space charge region becomes narrower with respect to the zero bias because this potential difference and potential barrier is reduced. Decreasing the potential barrier causes a lower concentration of majority carriers, and therefore, the flow of majority carriers occurs to offset the decline. A net current flows under forward bias across the p-n junction due to low resistance. Thus, the p-n junction diode with low resistance behaves as a short circuit [33, 34, 36].

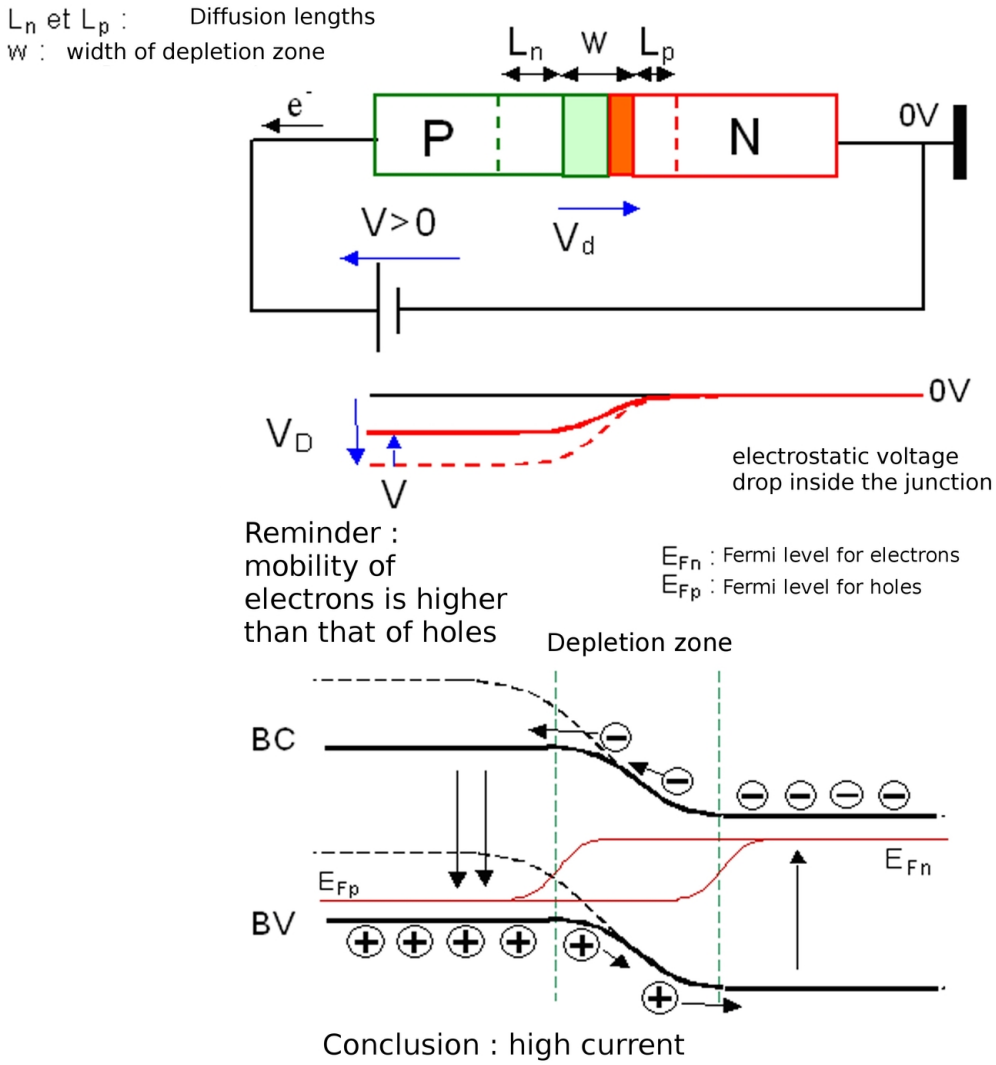


Figure 1.4 The p-n junction diode under forward bias [38]

1.1.3 The p-n Junction Under Reverse Bias

When the p-n junction diode is under a reverse bias condition, a p-type semiconductor is linked with a negative voltage terminal and an n-type semiconductor is connected to a positive voltage terminal (presented in Figure 1.5). Unlike the forward bias, electrons in the n-region and holes in the p-region move away from the junction, which results in an applied voltage increase to the potential difference. This causes high resistances against the flow of the charge carriers. The p-n junction diode with high resistance behaves as if it is an open circuit. Because of

this, there is no flow of current through the p-n junction. Correspondingly, the space charge region under the reverse bias will be larger than the zero bias [34, 36, 37].

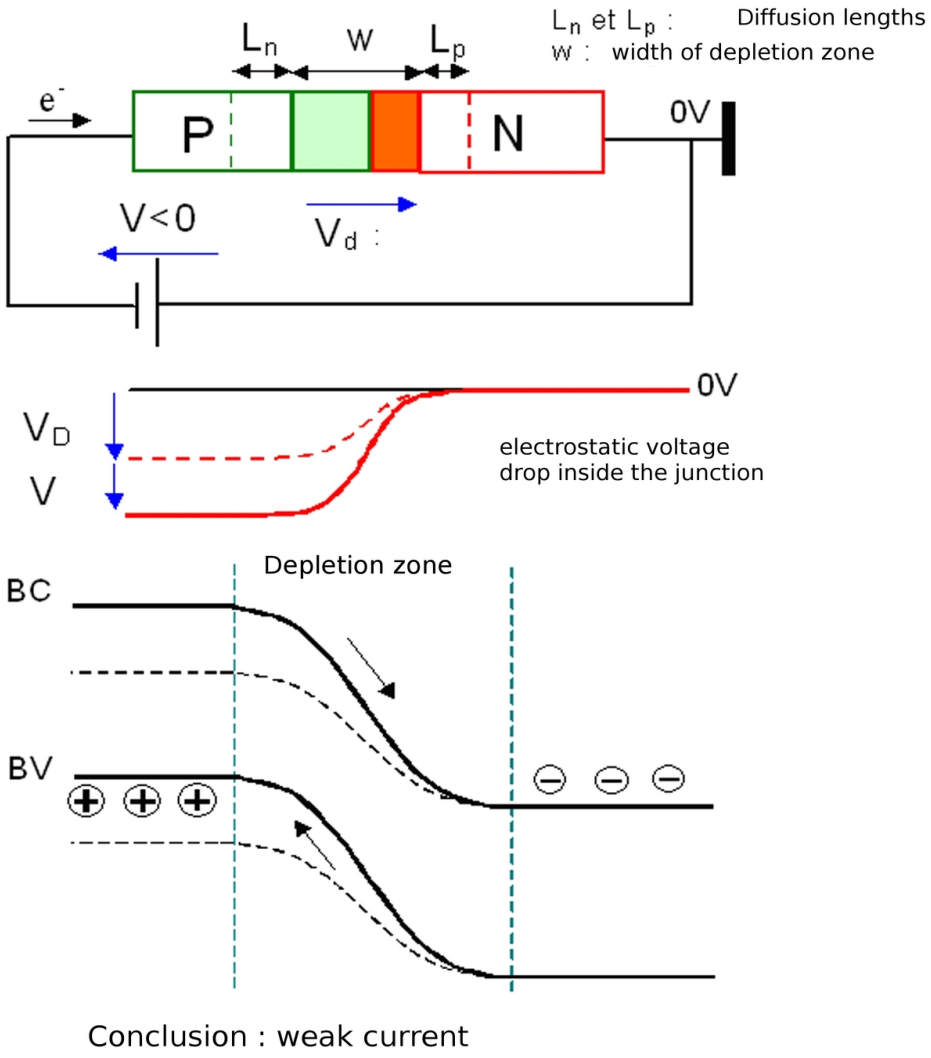


Figure 1.5 The p-n junction diode under reverse bias [38]

1.1.4 The p-n Junction Diode Under Illumination

When the p-n junction diode is under illumination, it absorbs photons. The absorption of photons will generate electron-hole pairs in the semiconductor material, and this affects the minority charge carriers, which means that light excites

the charge carriers and strongly increases the concentration of minority carriers that are holes in the n-region and electrons in the p-region. This augmentation gives rise to the flow of holes from the n-region to the p-region and the flow of electrons from the p-region to the n-region, which is called photo-generation current, I_{ph}. By illuminating the p-n junction, the electrical current can be obtained on the external circuit by short-circuiting electrodes. This current is called a short circuit current (I_{sc}). Also, I_{sc} is described as the maximum current. If there is no external contact, there is no current flow, which is called open circuit voltage (V_{oc}). The V_{oc} is referred to the maximum voltage as well [33].

1.4 Photodiodes

Photodiodes, one kind of photodetector, are light sensing devices that convert incident light into electric current. Photodiodes operate in the space charge region of the p-n junction with applied reverse biased voltage.

1.5 Fundamental Working Principles of Photodiodes

Fundamental working principles of photodiodes are based on photoconductive or photovoltaic effects. For the semiconductor photodiode devices consisting of p-n, the junction under reverse bias absorbs the incident photon, which is loaded energy on them, when the energy of incident light is the same or higher than the bandgap energy of semiconductor. With the energy of incoming light, electrons in the valence band with a lower energy level have the energy to break their covalent bonds and transition into the conduction band with a higher energy level. This process generates electron-hole pairs in the space charge region. These electron-hole pairs lead to increased mobile charge carriers, so conductivity is increased; thus, *the photoconductivity effect* is an optical and electrical phenomenon in which a material becomes more electrically conductive under the action of light. Also, *the photovoltaic effect* operates under the zero bias in the p-n junction. The dark current is limited to an increase in the photosensitivity of the device and a voltage occurs. Moreover, with the photoconductivity or photovoltaic effect, photodiodes are used to determine the presence of light. [39-41].

1.6 Equivalent Circuit

Figure 1.6 demonstrates the equivalent circuit of a photodiode. The abbreviations are as follows: I_L is the photocurrent, I_D is diode current, C_j *is* junction capacitance, R_{sh} is shunt resistance, R_s is series resistance, I' is *s*hunt resistance current, V_D is diode voltage, V_o is output voltage and I_o is output current expressed by equation (1.1),

$$I_0 = I_L - I_D - I' = I_L - I_s\left(exp\frac{q\,V_D}{kT} - 1\right) - I' \ldots \qquad (\mathbf{1.1})$$

where I_s is the saturation current, q is electron charge, k is the Boltzmann's constant and T is the absolute temperature of the photodiode.

The output current is the short circuit current (I_{sc}) in the photodiode when R_L=0 and $V_o = 0$, and I_{sc} is given by equation (1.2):

$$I_{sc} = I_L - I_s\left(exp\frac{e.(I_{sc}R_s)}{kT} - 1\right) - \frac{I_{sc}R_s}{R_{sh}} - \cdots \qquad (\mathbf{1.2})$$

For high-quality photodiodes, the value of R_s is several ohms and the value of R_{sh} is 10-10^5 MΩ. Herein, the second and third terms in equation (1.2) can be ignored in quite a wide range, and the output current (I_0) will be equal to the photocurrent (I_L).

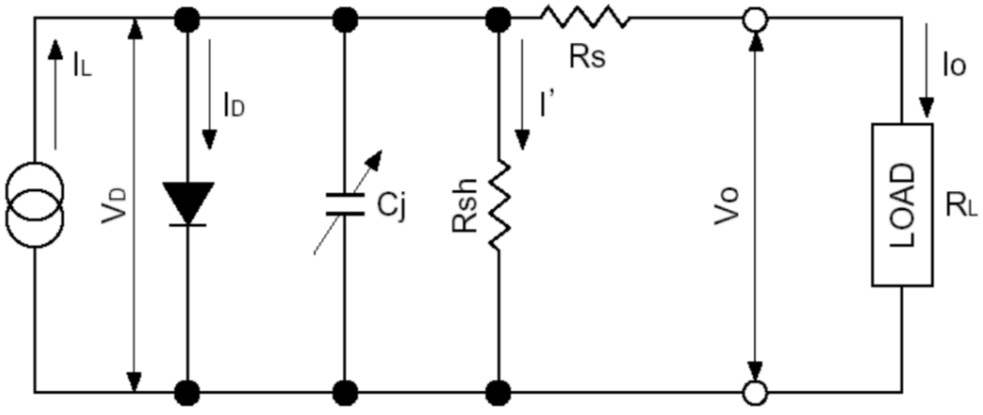


Figure 1.6 Equivalent circuit of a photodiode [42]

The output voltage is the open circuit voltage in the photodiode when $I_0 = 0$, and V_{oc} is expressed by equation (1.3):

$$V_{oc} = \frac{kT}{q} ln\left(\frac{I_L - I'}{I_s} + 1\right) ... \quad (\mathbf{1.3})$$

When I' is a negligible term, V_{oc} is inversely proportional to temperature and proportional to $ln(I_L)$ because I_s exponentially increases with temperature. However, this photodiode does not work when detecting poor light [42, 43].

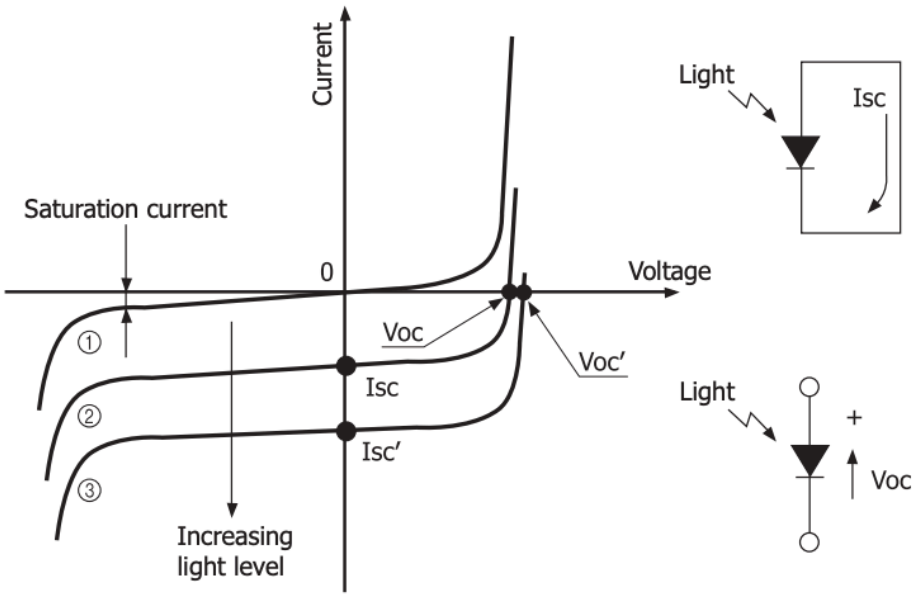


Figure 1.7 The current-voltage characteristics of a photodiode with Voc and Isc [43]

The current-voltage (I-V) characteristics of a photodiode are presented in Figure 1.7. The photodiode exhibits rectifying p-n junction diode behavior in the dark, such as level 1 in Figure 1.7. The dark current equation is provided by equation (1.4):

$$I_D = I_s\left[exp\left(\frac{qV_A}{nk_BT}\right) - 1\right] \quad (\mathbf{1.4})$$

where I_s is the saturation current, q is the charge carriers (1.60 x 10^{-19}), V_A is the applied voltage, k_B is the Boltzmann's constant (1.38 x 10^{-23} J/K), n is the ideality factor and T is the absolute temperature. When the photodiode is illuminated using a

light source, the current-voltage characteristics are altered as much as the amount of I_{ph}, which is the photocurrent. I_{ph} is given as equation (1.5) [44]:

$$I = I_s \left[exp\left(\frac{qV}{nkT}\right) - 1 \right] - I_{ph} \qquad (\mathbf{1.5})$$

When incident light strikes the photodiode, the light level is increased from level 1 to 3 as illustrated in Figure 1.7.

1.6 The Applications of Photodiodes

The applications of photodiodes are the same as the other types of photodetectors. The photodiodes are used to alter the state of circuitry, either for digital signal processing or switching and control. In addition to these digital applications, there are other applications used to produce an output that is dependent on light, which for measurement is called analog application. The photodiodes are utilized for light measurement, such as camera light meters. They are used to provide a reaction to the intensity of lights in the switching on the street lighting following dark as well. They are also used for smoke detectors, which are safety equipment. In addition, they are the devices in air conditioners and television receivers for infrared remote controls. Photodiodes are used to determine the exact measurement of intensity of light because they generally have rather linear responses. In some circuitry, they are combined with light emitter devices (LED) to detect different product types depending upon their optical absorbance. Also, in medicine photodiodes have many applications, such as blood gas monitoring, analyzing samples and detecting computed tomography. Some kinds of photodiodes are so fast they are utilized for optical communication applications. In addition to these fields, photodiodes are generally used as bar code scanners, position sensors and in compact disc players [41].

1.7 Literature Review

Huang et al. (2018) [20] produced both ZnO on p-Si and boron gallium ZnO (BGZO) on p-Si heterojunction diodes by means of the magnetron sputtering method and gold (Au) ohmic contacts, which were applied to the top side of a device. Under

UV light with 365 nm wavelength, the BGZO device produced more photocurrent and small dark current; therefore, the BGZO device had a better photosensitivity value, roughly 490, than that of pure ZnO, which was about 47.

Tsay et al. (2017) [45] compared the electrical behavior of sol gel derived from AZO, GZO and undoped ZnO on glass substrates. The GZO photodetector indicated strong photoelectrical conversion ability, meaning that the photosensitivity (I_{UVA}/I_{dark}) was 73.3 at 5 V when compared to others under UVA light with a power of 0.825 mW/cm^2.

Zhou et al. (2017) [46] evaluated photoresponse performance of a GZO nanorods/p-GaN heterojunction photodetector device and ZnO nanorods/p-GaN heterojunction photodetector devices under UV light with a power of 1.31 mW/cm^2. As in the GZO nanorods, gallium reduced the imperfections and increased photogenerated carrier transmission and conductivity of the ZnO film; device performance was improved over the undoped ZnO photodetector device, when photosensitivity at zero bias was compared.

Young et al. (2016) [47] produced a photodetector using grown GZO nanorods on ZnO seeds/glass substrate with the hydrothermal growth technique. The contacts of the photodetector were Au. As a result of the current-voltage measurement in the dark and under UV illumination with a 365 nm wavelength, a photosensitivity value (I_{ph}/I_{dark}, denoting the ratio of photocurrent and dark current) of this fabricated photodetector of about 15.2 at 1 V was obtained.

Akgul et al. (2016) [48] examined photovoltaic properties of a GZO/Si nanowires (NWs) heterojunction diode by the RF magnetron sputtering method under AM1.5 G (80 mW/cm^2). Au on the top contacts and Al on the bottom contacts were made by using the thermal evaporation method. The rectification ratio (I_F/I_R, denoting the ratio of forward current and reverse current) of this structure was approximately 100 at $\pm$1 V.

Lin et al. (2013) [49] investigated a GZO/p-Si diode in terms of electrical properties, and they fabricated the diode by means of the RF magnetron sputtering method with

aluminum on the top and bottom contacts. The saturation current density of the diode was calculated by using thermionic emission theory and was found to be 1.92×10^{-3} A/cm^2, which is a remarkably high value.

Yang et al (2011) [50] studied the GZO nanorods/ZnO seed layer/p-Si, which had Ti/Au front contacts and Al back contacts produced by thermal evaporation. In brief, this structure demonstrated a diode behavior with a Ga/Zn ratio of 0.2.

CHAPTER 2

DEVICE FABRICATION

Figure 2.1 illustrates the structure of a n-GZO/p-Si heterojunction photodiode. The designed structure was produced step by step in this study. The p-type silicon substrates were selected as a device absorption layer. Also, the GZO layer was selected with high transparency as a device emitter layer. The top and bottom contacts were silver (Ag) on the surface and the backsides of the Si substrates as displayed in Figure 2.1. Under AM1.5 solar light, devices were characterized. Experimental details are given in this chapter.

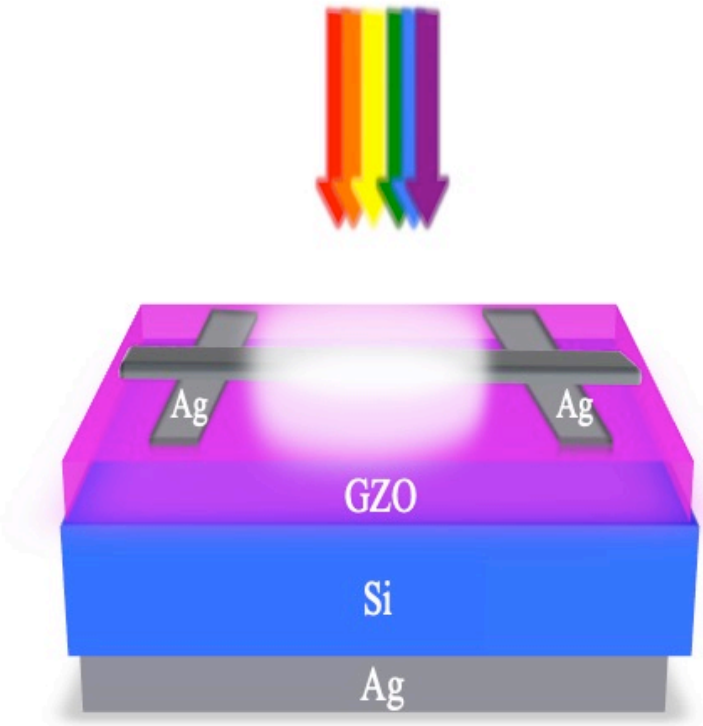


Figure 2.1 The fundamental structure of the photodiode

2.1 The solution preparation for ZnO: Ga

The solution of n-type Ga doped zinc oxide (GZO) to be coated on the top surface of the silicon substrates was prepared. In this experiment, the materials used for the preparation of the n-type coating solution were zinc acetate dihydrate, ZAD ($ZnC_4H_6O_4.2H_2O$; Emsur) as the precursor source of the zinc material, gallium nitrate hydrate ($Ga(NO_3)_3.xH_2O$; Aldrich, 99.9 % purity) as the dopant, ethanol (CH_3OH; Emsur) as the solvent and monoethanolamine (C_2H_7NO; Emsur, 99.5 % purity) as the stabilizer.

In this study, the parameters presented in Table 2.2 were utilized to fabricate the p-n junction photodiode. The molar ratio of zinc acetate dihydrate to monoethanolamine had equal molarities and concentration of zinc acetate dihydrate to ethanol was 0.2 M (mol/l). In addition, the Ga dopant concentration ([Ga]/[Ga + Zn]) was 2 at. %.

Table 2.1 The quantities used for the chemical solution

Materials		**Quantities**
The precursor	Zinc acetate dihydrate (ZAD)	1.098 g
The dopant	Gallium nitrate hydrate	0.026 g
The stabilizer	Monoethanolamine (MEA)	0.312 g
The solvent	Ethanol (EtOH)	25 mL

First, as Table 2.2 indicates, zinc acetate dihydrate (ZAD) had a given weight value of 1.098 g and was dissolved in 5 ml ethanol in a magnetic stirring for 15 minutes at room temperature (number 1 in Figure 2.2). At the same time, the same procedure was applied for is 0.026 g of gallium nitrate hydrate (number 2 in Figure 2.2) and 0.312 g of monoethanolamine (MEA) (number 4 in Figure 2.2) dissolved in 5 ml ethanol in a magnetic stirring for 15 minutes at room temperature. At the end of the specified period, the solution in which the precursor and dopant materials were

present was stirred in a beaker for 15 minutes at room temperature using magnetic stirring (number 3 in Figure 2.2). Finally, these solutions, indicated in numbers 3 and 4 in the Figure 2.2, were stirred in a beaker for 2 hours at room temperature using a magnetic stirrer (number 5 in Figure 2.2). After obtaining homogeneous, clear and transparent solutions, the solution was subjected to an aging process for 24 hours in ambient air.

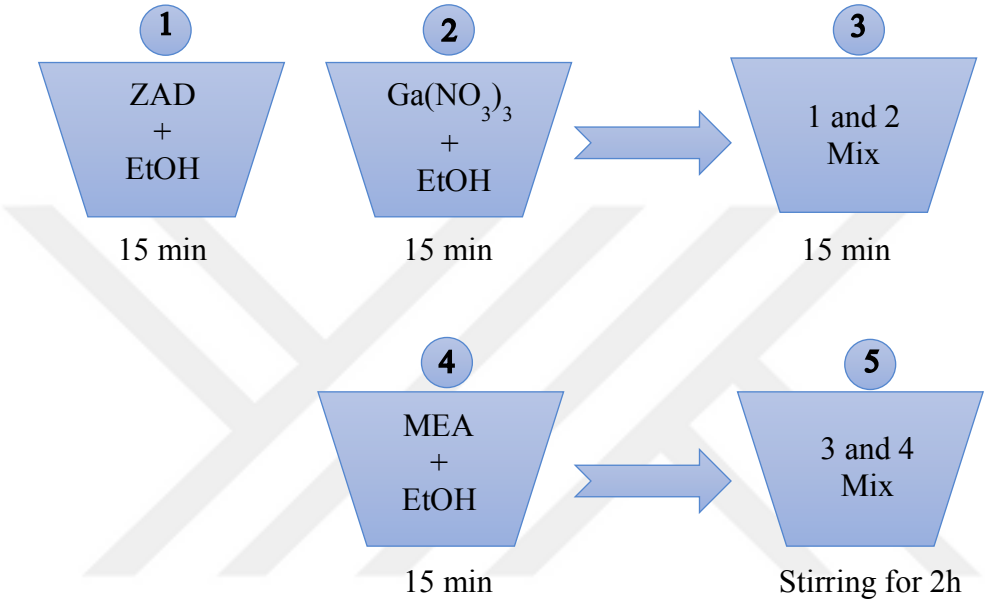


Figure 2.2 The n-type GZO solution preparation process

2.2 Cleaning Process for Si Substrates

The cleaning process for the silicon substrates that had single crystal p-type orientations, 1–20 Ω.cm resistivity and 525 μm thickness occurred in four stages, as illustrated in Figure 2.3, before the GZO film was deposited on the top surface of the silicons. Protective gloves and a special mask were used to prevent adverse health effects and to ensure safe application of this process.

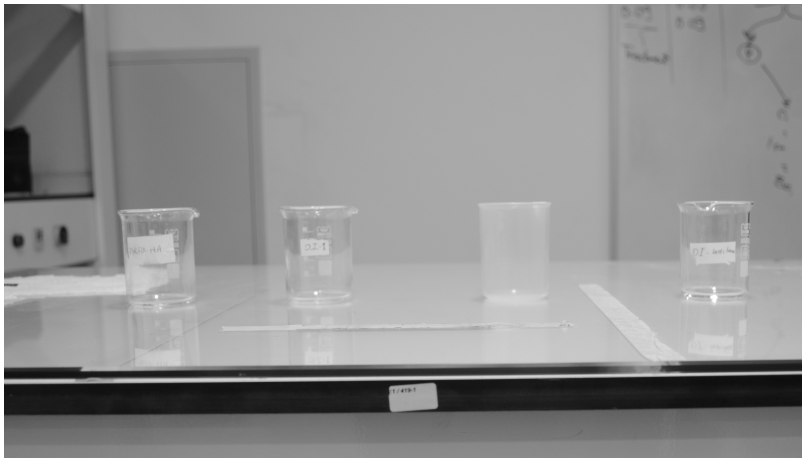
1. **Piranha cleaning standard:** The first method used to clean the silicon substrates was the piranha clean standard. After taking necessary precautions, the 3:1 ratio of a mixture of 45 mL sulfuric acid (H_2SO_4, 96 % purity) and 15

mL hydrogen peroxide (H_2O_2, 30% purity) was mixed in a glass beaker. Right after combining the chemicals, the silicon substrates were dipped in the mixture of sulfuric acid and hydrogen peroxide for 15 minutes to eliminate the organic and inorganic contaminants.

2. **HF (2%) dip (HFDIP):** Hydrofluoric acid (HF, 30% purity), present in the laboratory, was diluted to 2% ratio using deionized water in the polypropylene beaker. The amount of 30% hydrofluoric acid (HF) used for the dilution procedure was 3.75 ml, and the amount of deionized water was 56.25 ml. When the dilution procedure was complete, silicon substrates were soaked in the dilute HF for 5 minutes. Dilute HF was utilized to clear off the native oxide layer, called SiO_2.

3. **The rinsing process:** After the Piranha Clean Standard was performed, silicon substrates were rinsed in the deionized water for 2 minutes.

4. **The drying process:** Silicon substrates, which were wet after the cleaning process was complete, were put into the furnace (OptoSense) at 150 ℃ for 5 minutes to dry them**.**



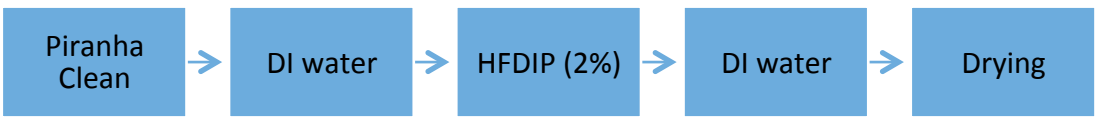


Figure 2.3 The cleaning process for Si wafers

2.3 Deposition

Following the overnight aging process of the Ga-doped ZnO solution, the GZO solution, with 0.2 M and 2% at Ga, was dropped onto the entire surface area (1.5 x 1.5 cm^2) of the p-type silicon substrates using a stactometer. Silicon substrates rotated at a speed of 2000 rpm for 30 seconds, with an acceleration time of 2 seconds and a deceleration time of 5 seconds, to yield the n-GZO/p-Si junctions by means of using the spin process controller device (Spin-1200 T, MIDAS Co. Ltd, Korea), displayed the Figure 2.4. After each spin coating process, Ga-doped thin films, which were 0.2 M, were dried at 500 ℃ for 5 minutes in a tube furnace so that the solvent would evaporate and organic materials could be eliminated from the films on the silicon substrates (presented in Figure 2.5). In the meantime, the deposition process of GZO thin films, which was performed for the silicon substrates, was completed on the small piece of split glass (1.5 x 1.5 cm^2) surface in order to measure the absorbance and transmittance. This deposition process was performed at different cycles (1, 3 and 5), and so three different Ga doped thin films with different thicknesses were obtained. Then, thin films were annealed in ambient air in a tube furnace at 500 °C for an hour. The thickness of the GZO thin film on the silicon substrates obtained was approximately 35 nm for each cycle performed.

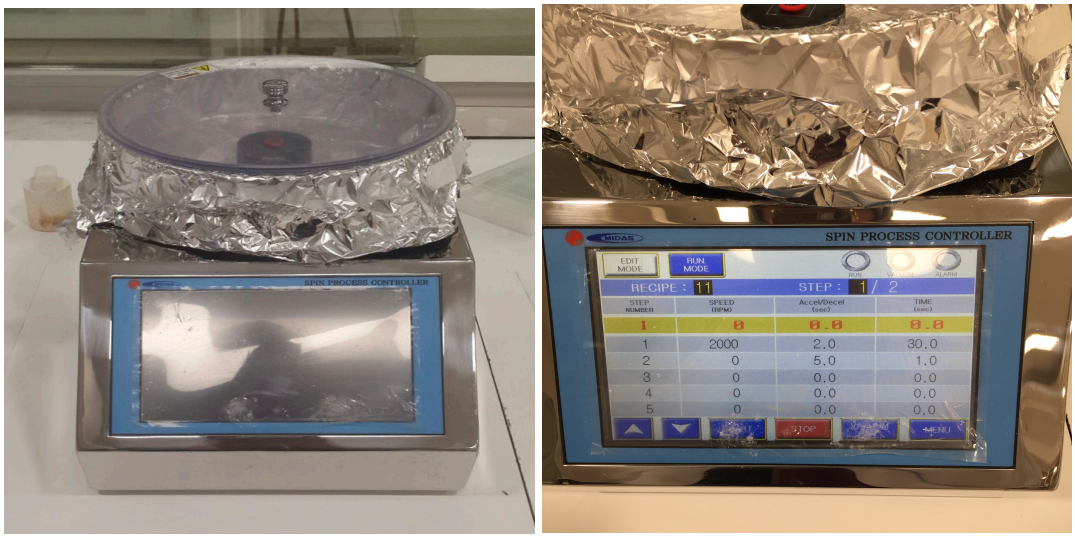


Figure 2.4 The picture of the spin coater used for preparing thin films

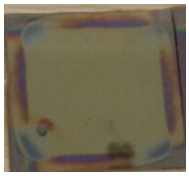


Figure 2.5 The picture of GZO thin film on p-silicon after the deposition process

2.4 Metallization

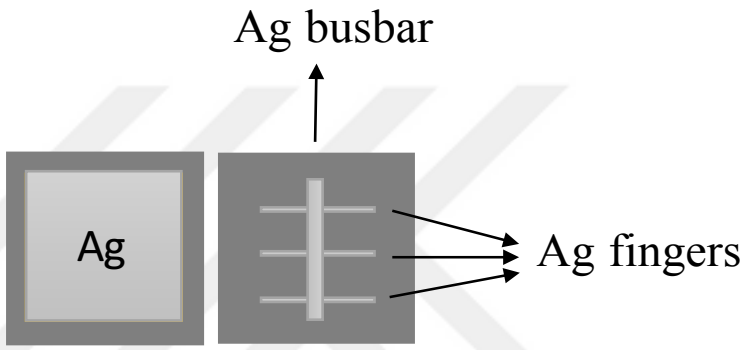


Figure 2.6 The rear silver contact (left) and the top silver contacts (right)

The front contact and backside contact were applied using silver (Ag) paste (Aldrich). First, before the deposition of the GZO layer, the back silver contact of silicon substrates was applied to a square area of 1 x 1 cm^2 on the bottom of the silicon substrates (depicted in Figure 2.6). The silicon substrates, which had back contacts made using silver paste, were inserted into the tube furnace at 150 °C to dry the contacts for 5 minutes.



Figure 2.7 After the metallization, silicon substrates with different thicknesses

After the deposition process of the GZO layer, the front contacts of the silicon substrates were made in two steps. The first step was making three thin lines, called fingers; the second step was the making a wider line called a busbar (illustrated in Figures 2.6 and 2.7). The fast annealing process, called the firing process, was implemented at 810℃ for 20 seconds using the tube furnace.

CHAPTER 3

DEVICE CHARACTERIZATION

The experiments for the determination of the structural, optical, electrical and morphological properties of the GZO/p-Si heterostructure photodiodes were carried out in the Laboratory of the Department of Energy Systems of the Ankara Yıldırım Beyazıt University. (AYBU). X-Ray Diffraction (XRD), Atomic Force Microscopy (AFM) and UV-VIS-NIR spectrophotometer were utilized to examine the structural, morphological and optical properties of the samples. The Scanning Electron Microscopy (SEM) measurements of the samples were implemented in the central laboratory of Middle East Technical University (METU). The thin film thicknesses of heterostructure photodiodes were determined by the SEM. Ultimately, the rectifying and photosensitivity behavior of the photodiode was determined by using the current-voltage (I-V) measurements.

3.1 X-Ray Diffraction Measurements



Figure 3.1 XRD measurement device (Rigaku Miniflex 600 Table)

Figure 3.1 illustrates the XRD measurement device (Rigaku Miniflex 600 Table) used in this study to determine the structural properties of materials. The diffraction patterns were obtained between 25 and 65° with a step size of 0.02° using Cu-K_α radiations, and they were analyzed using PDXL software. The working principle of XRD is based on Bragg's Law [51],

$$n\lambda = 2d \sin\theta \qquad (\mathbf{3.1})$$

where n is the order of reflection, λ is the X-ray of the wavelength, d is the interplanar spacing and θ is measured between the incident beams and is called Bragg's angle. X-ray diffraction techniques were used to identify the crystal phases of various materials after the detection of lattice parameters and to determine the average grain size and direction of grains.

3.2 Atomic Force Microscopy Measurements

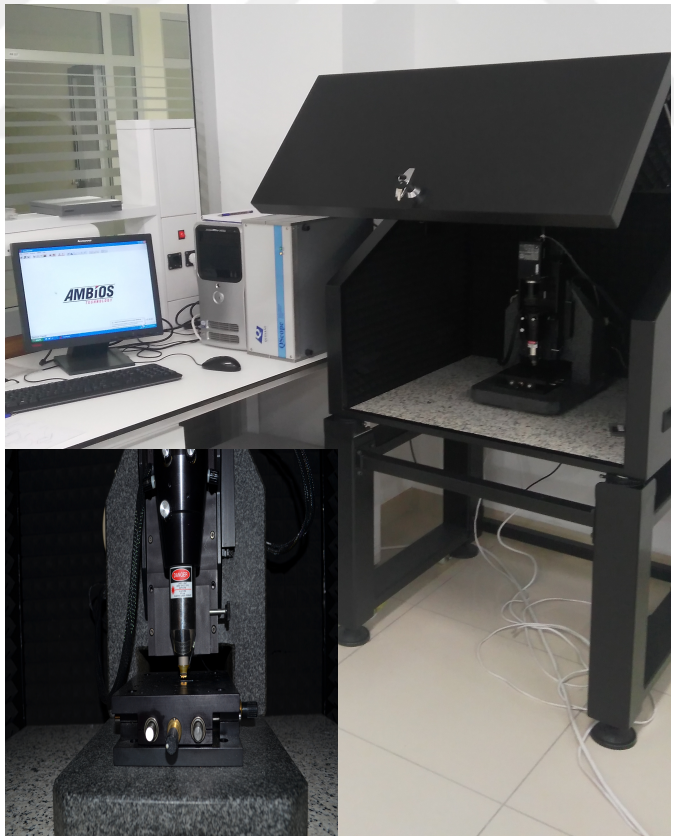


Figure 3.2 AFM measurement device (Quesant Ambious Q-scope series)

The surface morphology of materials was investigated using the Atomic Force Microscopy (AFM) device displayed in Figure 3.2. The AFM provides both image 3D topography and type of surface measurements and is a microscope that can display surface morphology on the order of Angstrom (Å). This microscope consists of a cantilever with a sharp tip, a photodetector, a laser and a scanner. The cantilever scans the surface of the materials, and the tip approaches the material's the surface. The attractive and repulsive forces happen in the cantilever. The laser notices positive and negative movement of the cantilever. As this cantilever scans the surface, topography is produced. The computer can monitor this topography. There are three operation modes for AFM. The contact mode can damage the materials because of the cantilever's movement. However, the tapping creates less damage to the material than the contact mode. Finally, the non-contact mode does not touch the material [52, 53].

3.3 The Scanning Electron Microscopy Measurements



Figure 3.3 SEM measurement device (QUANTA 400F Field Emission SEM)

The SEM, presented in Figure 3.3, is a measurement tool that focuses the beams of electrons. As a result of SEM measurements, morphological, topographical and compositional information about the material can be obtained. Also, these measurements can provide information about surface pollution, thickness of materials, crystal structure and smoothness of surface. Solid materials, especially, are characterized by the SEM. Materials can be imaged in a scanning mode using SEM techniques with the help of magnification ranging from 20X to approximately 30000X (spatial resolution of 50 to 100 nm) [54].

3.4 UV-VIS-NIR Measurements

Figure 3.4 illustrates the UV-VIS-NIR spectrometer (Shimadzu Corporation UV–1700), which measures a material's absorption, transmission and reflections versus specific wavelength. This spectrometer can detect the transparency of a material in term of percentage. In addition, due to the absorption in terms of arbitrary unit (a.u), a band gap calculation is possible for materials [55].



Figure 3.4 The UV-VIS-NIR Shimadzu Corporation UV-1700

3.5 Current-Voltage Measurements

Figure 3.5 demonstrates the Keithley 2400 SMU source meter with a solar simulator device (Abet LS 150, Abet Technologies, Inc., USA), which has AM1.5 (1000 W/m^2) irradiation. This meter is used to determine the electrical properties of heterojunction photodiodes with the help of their I-V characteristics.

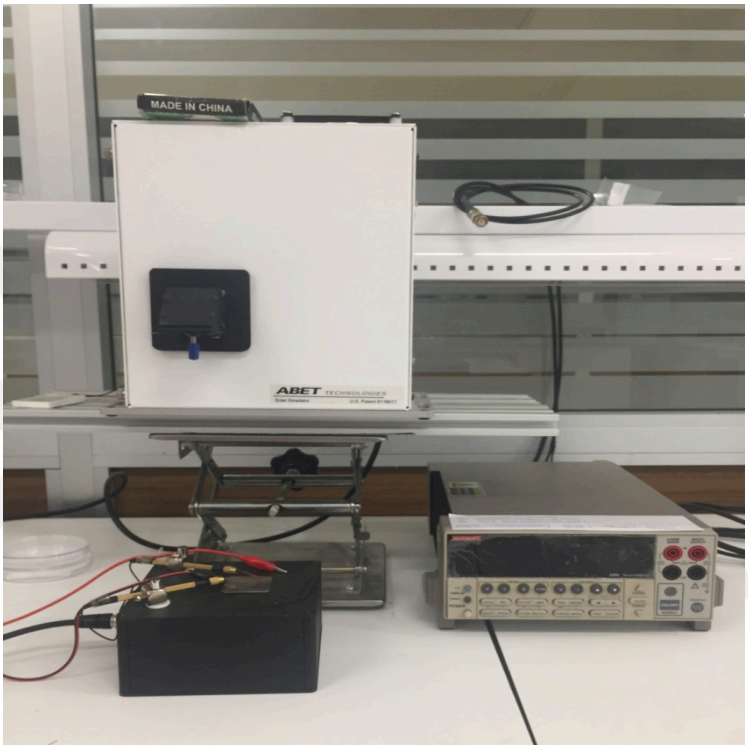


Figure 3.5 The Keithley 2400 SMU I-V measurement device with solar simulator

The current-voltage values taken from devices' contacts depending on the radiation from the solar simulator, were measured at room temperature with the help of the Keithley 2400 SMU source meter. The measured values were transferred to the computer software and the I-V characteristics were obtained.

CHAPTER 4

RESULTS AND DISCUSSIONS

This chapter presents the analysis of the electrical, morphological and optical characterizations of the photodiodes, which used the various characterization tools discussed in Chapter 3.

4.1 X-Ray Diffraction Results

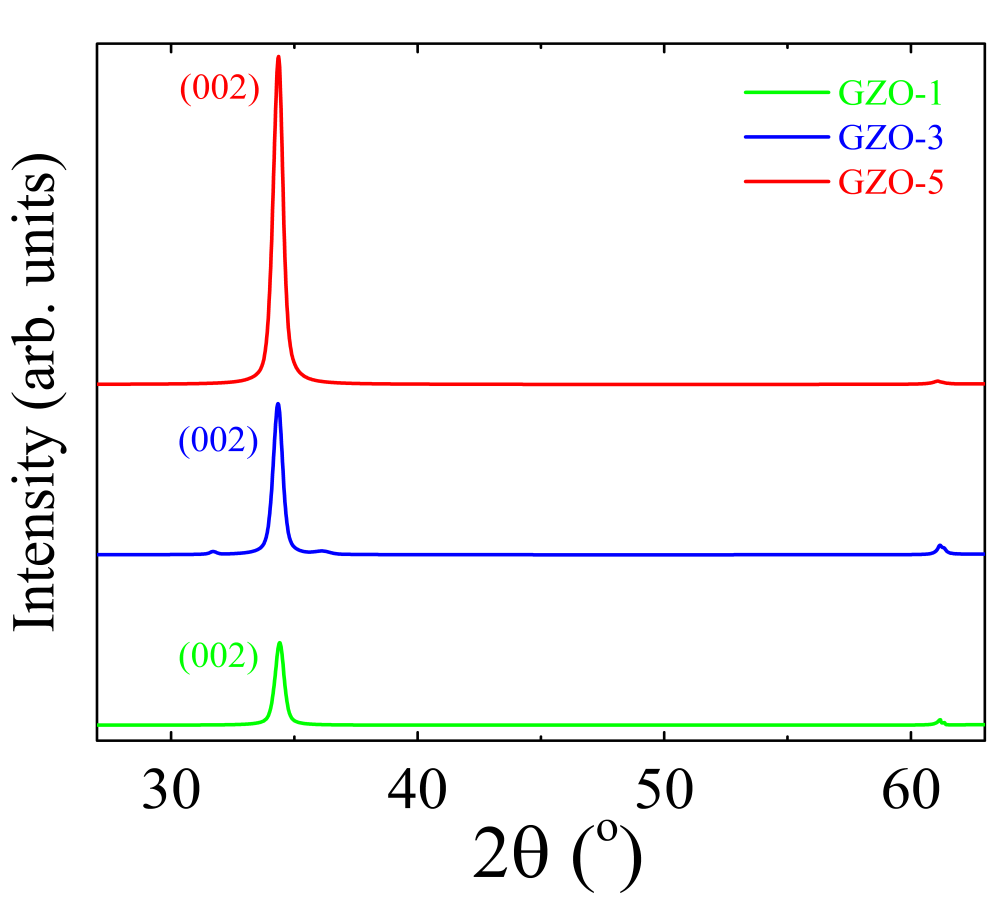


Figure 4.1 XRD results of Ga-doped ZnO thin films for different coating cycles

The XRD patterns displayed in Figure 4.1 belong to the GZO thin film, which had 0.2 M and 2% at. Ga deposited on the p-type silicon substrates of 525 µm thickness and <100> orientations for different coating cycles, such as 1-cycle, 3-cycle and 5-cycle, prepared by the sol-gel method. When the standard XRD pattern of the ZnO

crystal was considered regarding the standard JCPDS data file (No. 036-1451), it was determined that the thin films conformed to the hexagonal wurtzite structure of ZnO. The Bragg's diffraction angle range was in the 25 to 65° for 2θ at room temperature. As illustrated in Figure 4.1, there was a sharp diffraction peak with regard to (002) planes for the hexagonal wurtzite structure of the ZnO crystal pattern. The (100), (101) and (103) planes also were apparent in the XRD pattern, although they were relatively weak.

Table 4.1 List of 2θ, β, D for Ga-doped ZnO thin films for different coating cycles

Coating cycles	**2θ (°)**	**β (FWHM) (°)**	**D (nm)**	**TC**
1-cycle	34.40	0.38	23.04	3.58
3-cycle	34.34	0.41	21.47	3.51
5-cycle	34.35	0.42	20.83	3.96

The Scherrer's formula (equation 4.1) was used to calculate the average grain size (D) of GZO crystals coated in silicon substrates for (002) peak in the XRD patterns [51, 56]:

$$D = \frac{0.94\,\lambda}{\beta\cos\theta} \qquad (\mathbf{4.1})$$

where λ is the wavelength of the X-ray (1.5406 Å), β is the full-width at half-maximum (FWHM) of the (002) peak in radians, and θ is the Bragg's diffraction angle (reflection angle) of a strong XRD peak in radians. As present in the Table 4.1, 2θ, which is the diffraction angle, were found 34.40°, 34.34°, 34.35° and the β values were 0.38°, 0.40°, 0.42° from XRD patterns for 1-cycle, 3-cycle and 5-cycle, respectively. As the coating cycle increased, the average grain size diminished from 23.04 nm to 20.83 nm, as displayed in Table 4.1. The changing average grain size with varying thicknesses can be significant factor grain boundaries reduction [57-59]. The alteration in average grain size may have remarkable influence on the

capacity of the GZO/p-Si heterojunction photodiodes because the thinner film of the GZO device, which has a high crystallite size, is supposed to reduce the resistance due to diminishing carrier trapping at the grain boundaries [60].

The analysis of thin film texture at different thickness of ZnO thin film on Si was possible with the help of the texture coefficient (TC), which can be calculated using equation (4.2) for (002) plane [27]:

$$\mathrm{TC(hkl)} = \frac{\frac{\mathrm{I(hkl)}}{\mathrm{I_0(hkl)}}}{\frac{1}{\mathrm{N}}\sum_{\mathrm{n}}\frac{\mathrm{I(hkl)}}{\mathrm{I_0(hkl)}}} \qquad (\mathbf{4.2})$$

where I (hkl) is intensity of (hkl) plane measured for ZnO, N is the number of reflection, I_0 (hkl) is the standard intensity of a plane (hkl) obtained from the JCPDS data card of ZnO, and n is the number of diffraction peaks. The calculation for TC of (002) XRD peaks is given in Table 4.1. The high TC value is a measure of improved crystal structure [61]. The 5-cycle GZO thin film had a better crystal structure than the others when compared to TC. This TC value is related to roughness of the crystal surface. A changing roughness of surface affects TC [62].

The "d," or called the crystalline plane spacing, as displayed in Table 4.2, was estimated using equation (4.3) [51],

$$d = \frac{\lambda}{2\,sin\theta} \qquad (\mathbf{4.3})$$

where λ is the wavelength of the X-ray (1.5406 Å) and θ is the Bragg's diffraction angle of (002) peak. When the crystalline plane spacing of GZO films were calculated, the crystalline plane spacing of GZO films were found about equal and were larger than the crystalline plane spacing of ZnO powder (0.2603 nm). Therefore, defects such as lattice strains and interstitial defects caused GZO films to become longer in crystalline plane distances [63].

The "c," or the lattice constant of GZO thin films, as given in Table 4.2, was calculated along the c-axis using equation (4.4) [64],

$$\frac{1}{d_{hkl}^2} = \frac{4}{3}\left(\frac{h^2 + hk + k^2}{a^2}\right) + \frac{l^2}{c^2} \qquad (4.4)$$

where "a" and "c" are lattice constants, d_{hkl} is the crystalline plane spacing, and (h, k, l) are Miller indices. The "c" was about the same for all coating cycles. Further, strain (ε), as presented in Table 4.2, was calculated by using equation (4.5) [65],

$$\varepsilon = \frac{c - c_0}{c_0} \qquad (4.5)$$

where "c_0" is the 0.5205 nm. As the strain value was positive, there was tensile strain on the GZO samples [65]. If the strain values were negative, this value would demonstrate the existence of the compressive strain on the surface of the GZO samples.

Table 4.2 List of c, d, and ε for Ga-doped ZnO thin films according to coating cycles

Coating cycles	**Lattice strain (c)**	**d (nm)**	**ε (%)**
1-cycle	0.521	0.2605	0.088
3-cycle	0.522	0.2609	0.277
5-cycle	0.522	0.2609	0.248

4.2 Atomic Force Microscopy Results

Figure 4.2 indicates the two-dimensional (2D) and three-dimensional (3D) AFM images on the left-hand side and on the right-hand side, respectively.

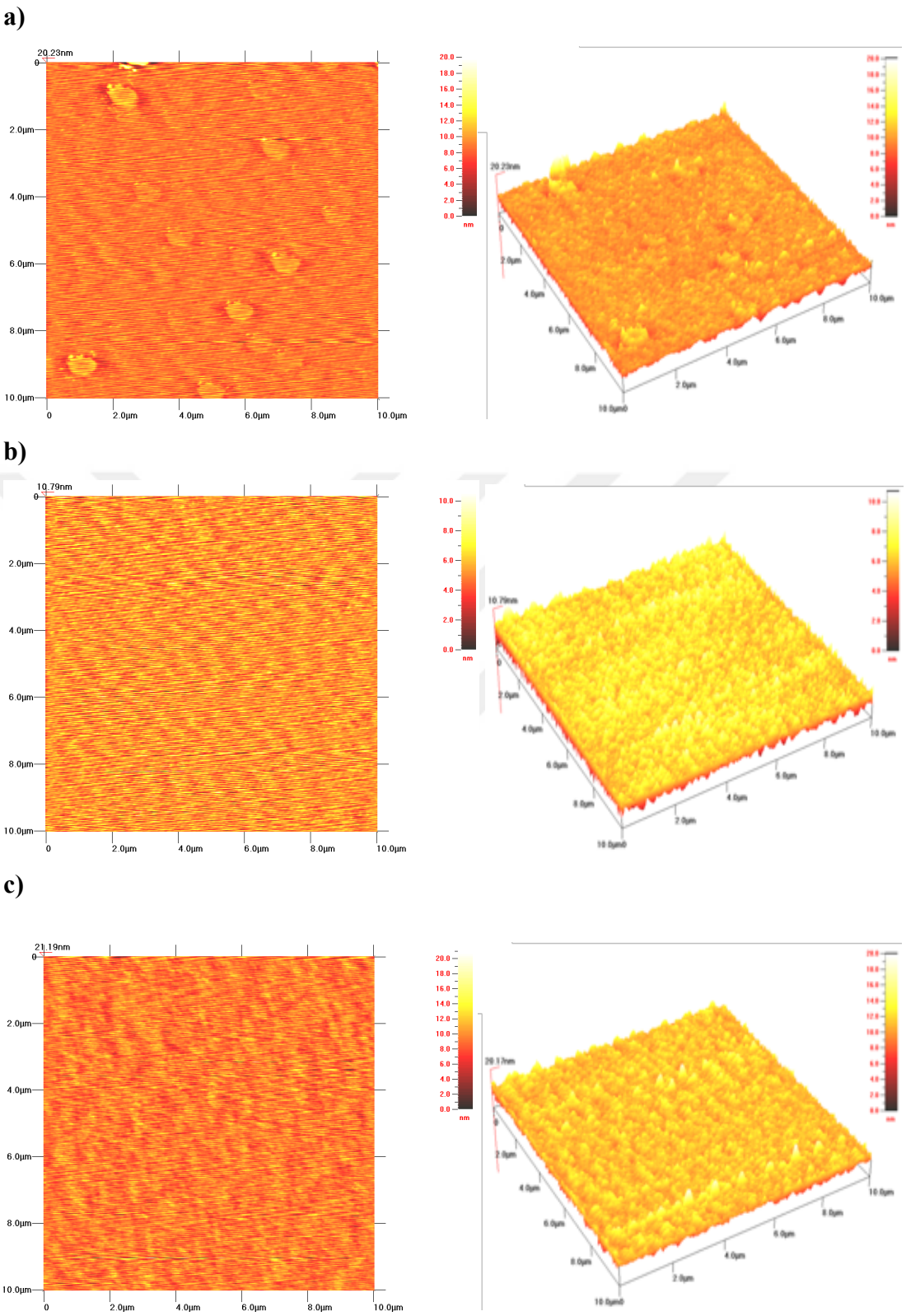


Figure 4.2 The 2-D (left) and 3-D (right) AFM images a) 1-cycle b) 3-cycle c) 5-cycle

These images indicate different thicknesses of GZO thin films. The surface root mean square (RMS) values of GZO thin films were extracted from the AFM images. As presented in Table 4.3, the RMS roughness values were 1.16 nm, 1.10 nm and 1.38 nm for 1-cycle, 3-cycle and 5-cycle, respectively. These values suggest that surface morphology is significantly uniform for GZO films; however, the RMS value, which had same trend as TC, as mentioned, is independent regarding thickness of the thin films. The RMS values were small when compared to the literature [43, 63, 65]. This smooth surface can outstandingly reduce the scattering of light hindered on the surface of the GZO device and develop the transmittance of the GZO device.

Table 4.3 List of RMS values

Sample	**RMS (nm)**
GZO-1	1.16
GZO-3	1.10
GZO-5	1.38

4.3 Scanning Electron Microscopy Results

The SEM micrographs of n-GZO/p-Si structure were measured at the Central Laboratory of Middle East Technical University (METU) via QUANTA 400F Field Emission SEM. Prior to the measurement of SEM images, GZO samples grown on Si substrates were properly cut and were coated with Au-Pd with 3 nm thickness in order to increase conductivity. The top and cross-sectional views were measured for n-GZO/p-Si thin films. The SEM measurements of the top views are displayed in Figure 4.3. In the top views, n-type GZO thin films deposited onto Si consisted of uniformly dispersed particles with a size of 23.50 nm, 27.09 nm and 33.63 nm, according to increasing thickness, as presented in Table 4.4.

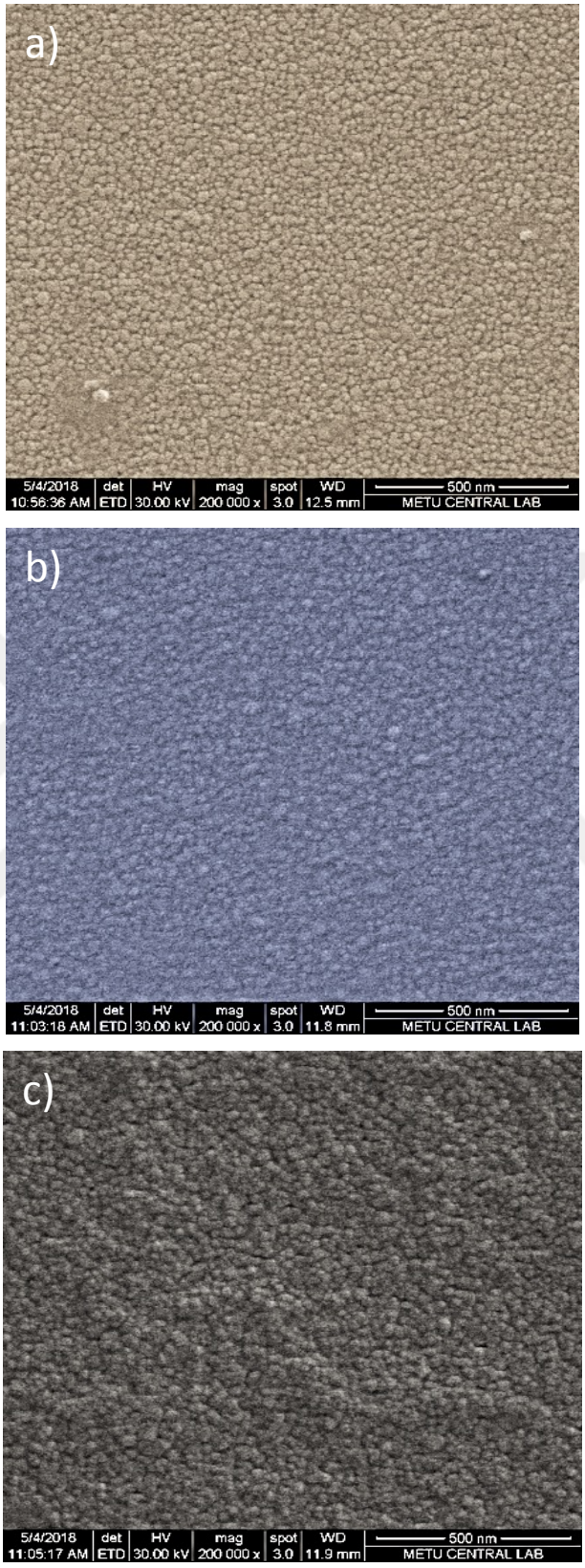


Figure 4.3 The top view of the SEM micrographs a) 1-cycle b) 3-cycle and c) 5-cycle

Table 4.4 The variation of particle size with thickness

Sample	Particle size (nm)
GZO-1	23.50
GZO-3	27.09
GZO-5	33.63

The particle size increased with increasing thickness of the GZO layer on Si substrates. The films had a dense structure and their particles were distributed homogeneously. Figure 4.4 indicates that cross-sectional micrographs of n-GZO/p-Si for 5-cycle were estimated at 177.9 nm. Therefore, the thickness was roughly estimated as 35 nm for 1 cycle.

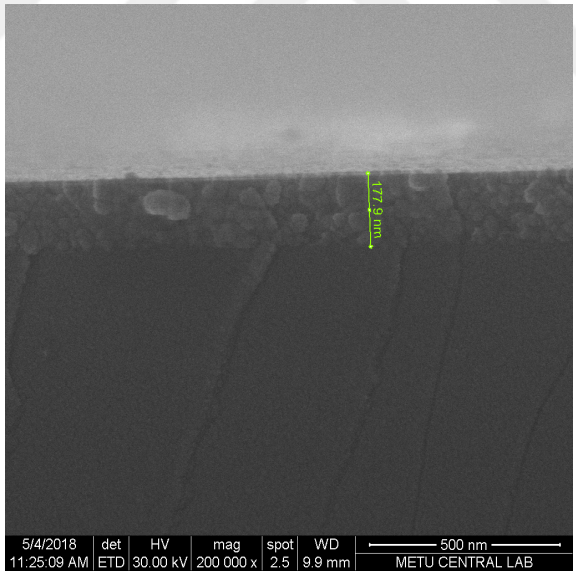


Figure 4.4 The cross-sectional view of the SEM micrographs for 5-cycle

4.4 UV-VIS-NIR Results

The optical properties were measured using Schimadzu UV-VIS-NIR 1700 Spectrophotometer for the n-type Ga doped ZnO grown on glass substrates at room temperature. Figure 4.5 illustrates the transmittance spectra of ZnO thin films deposited with Ga with various coating cycles. In the range of between 400 nm and 700 nm, the average optical transmittance was measured above 82 %, as presented in Table 4.5.

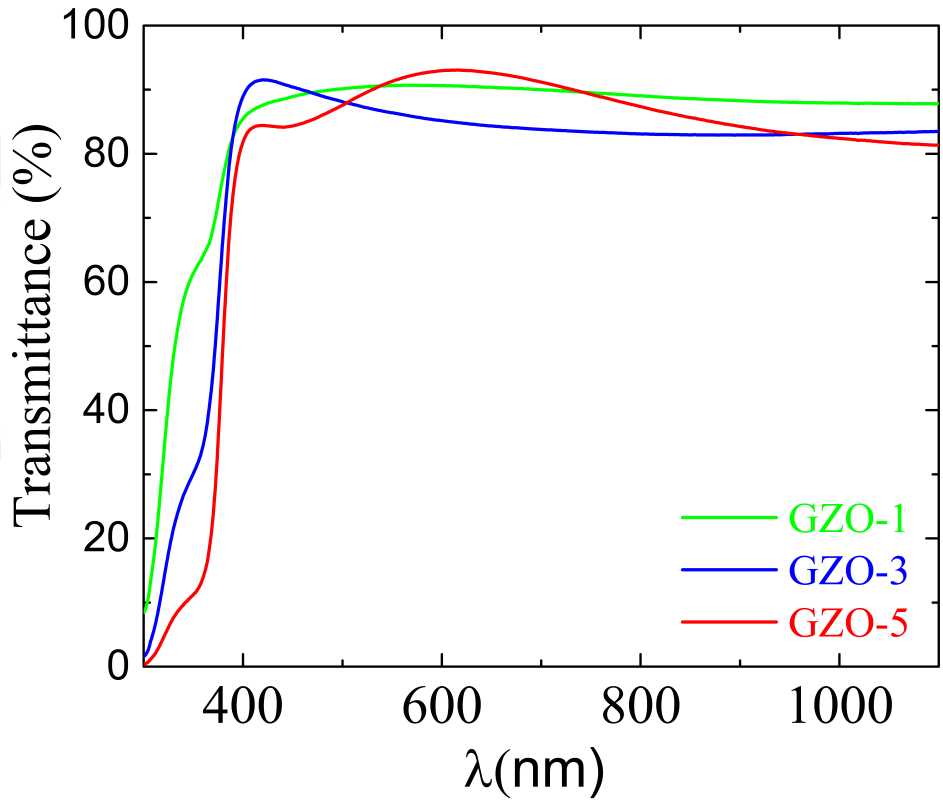


Figure 4.5 Transmittance spectra of ZnO thin films with various coating cycles

As a result, the films produced in different thicknesses were sufficiently transparent. The better transparency occurred in the thinner film and the worse transparency was apparent in the thicker film. The distortion increased with thickness, meaning optical and structural properties can be effected by thickness. The photons with lower-energy can penetrate the silicon layer because the devices' GZO layer allows their transition to this silicon layer. Photons, which arrive at the p-Si layer, are absorbed by the space charge region in this silicon layer [66]. In this absorber layer, the

electron-hole pairs are produced. Afterwards, these electron-hole pairs transform into photocurrents under the reverse bias. As a result, the GZO/p-Si heterojunction photodiode with the thinnest thickness, about 35 nm exhibited not only better transparency but also high crystal quality in all devices. Therefore, the highest photoresponse performance should be in this photodiode with 35 nm thicknesses.

Figure 4.6 demonstrates absorbance spectra of Ga-doped ZnO thin films for different coating cycles in the wavelength range of 300 nm to 1100 nm. The α as the absorption coefficient was extracted using Beer-Lambert's Law [67] from transmittance spectra,

$$\alpha = \frac{1}{d}\ln\left(\frac{1}{T}\right) \qquad (\mathbf{4.6})$$

where d is the thickness of the GZO thin films (about 35 nm for each cycle, determined from the SEM measurements), and T is the transmittance values for wavelength range of 300 nm to 1100 nm. The Tauc's relation [68] can be utilized to extract the energy band gap of n-type Ga-doped thin films grown on glass substrates in various thicknesses,

$$(\alpha h\nu) = A(h\nu - E_g)^n \qquad (\mathbf{4.7})$$

where α is absorption coefficient, $h\nu$ is the photon energy, E_g is the optical band gap and n is the constant determined from the type of direct allowed optical transition mechanism, which is 1/2 for ZnO material. Figure 4.7 illustrates $(\alpha h\nu)^2$ versus photon energy for GZO thin films for various coating cycles. The band gap value for GZO thin films with different coating cycle was obtained by extrapolating the slope $\alpha = 0$ in Figure 4.7 which is the $(\alpha h\nu)^2$ versus photon energy. As presented in Table 4.6, the optical band gap values were acquired as 3.205 eV, 3.267 eV and 3.272 eV according to increasing thickness. Increasing thickness of the GZO layer led to increases in the samples' band gap, which was attributed to the structural imperfections in the film lattices [69]. The values of the band gap were complied with the literature as reported by Tsay et al. (~3.25 eV) [27], Sbeta et al. (~3.28 eV) [64] and Serrao et al. (~3.270 eV) [70].

Table 4.5 List of average transmittances

Sample	T_{avg} (%)
GZO-1	87.4
GZO-3	82.8
GZO-5	82.5

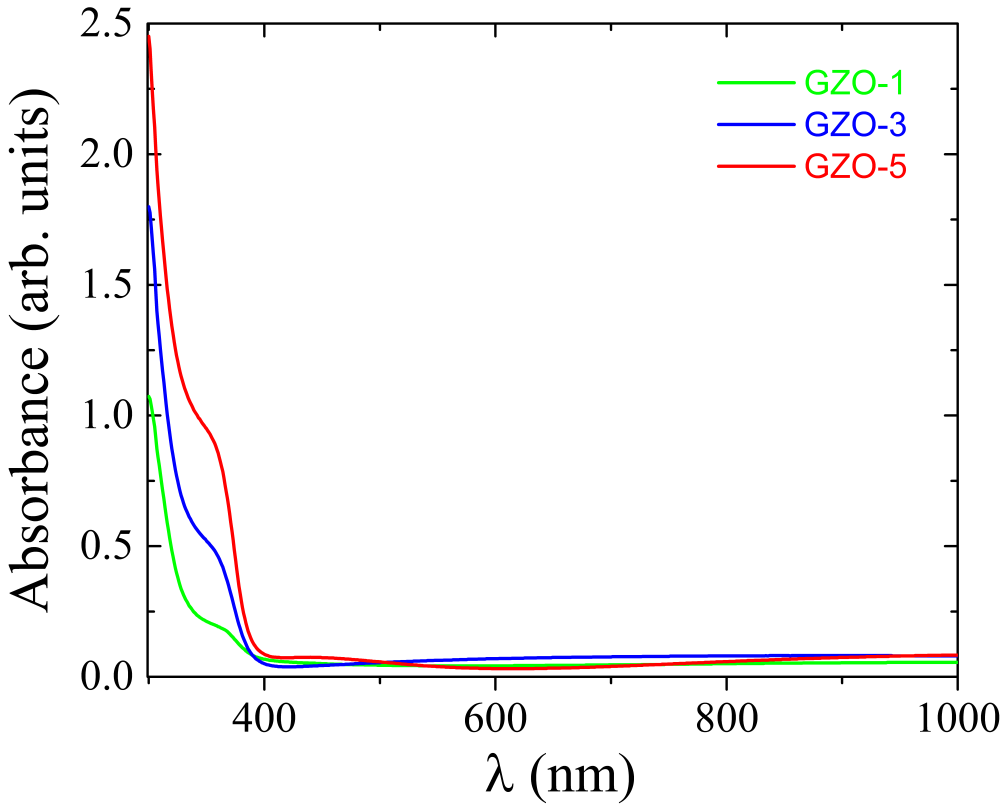


Figure 4.6 Absorbance spectra of Ga-doped thin films for different coating cycles

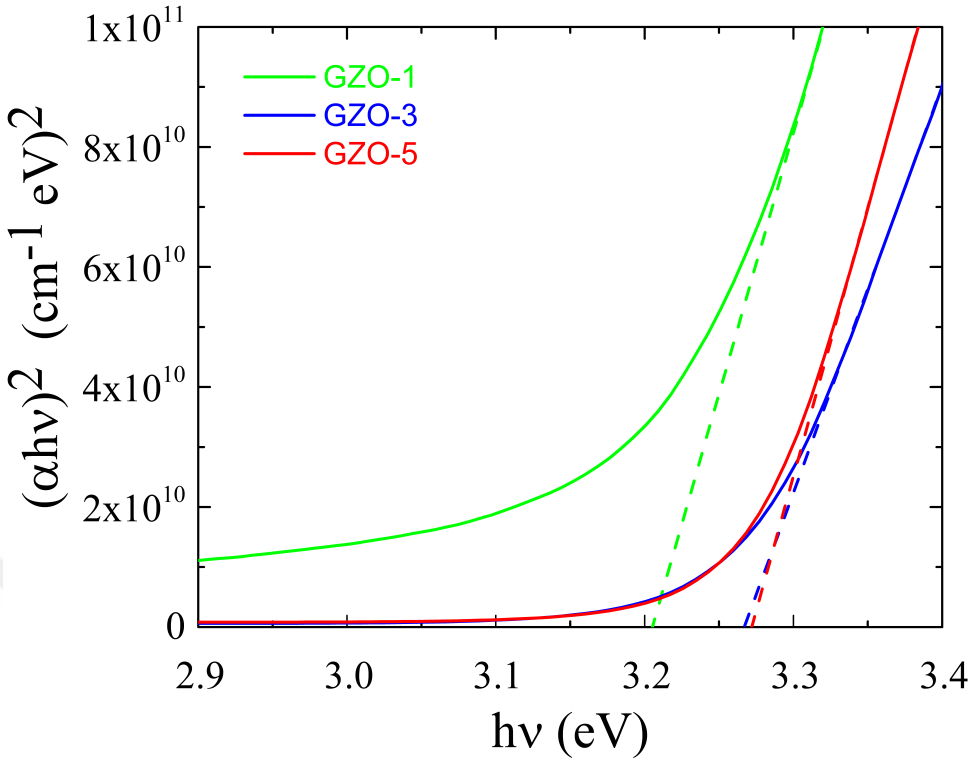


Figure 4.7 The $(\alpha h\nu)^2$ versus photon energy for GZO thin films on glass substrates

Table 4.6 List of band gaps

Sample	**Band gap (eV)**
GZO-1	3.205
GZO-3	3.267
GZO-5	3.272

4.5 The Current-Voltage Results

Figure 4.8 and Figure 4.9 demonstrate I-V curves of n-ZnO: Ga/p-Si photodiodes obtained by using the Keithley 2400 measurement device with light source, which

has 100 mW/cm^2, called AM1.5, at room temperature (300 K) for different thicknesses in dark conditions and under illumination, respectively. Also, Figure 4.10 illustrates the semilog I-V curves of the n-GZO on p-Si substrates with various thicknesses under illumination (AM1.5) and in dark conditions at room temperature. Regarding the general diode equation for photodiodes, the I-V characteristics are given as follows [71]:

$$\mathrm{I} = \mathrm{I_s}\left[\exp\left(\frac{\mathrm{qV}}{\mathrm{nkT}}\right) - 1\right] \qquad (\mathbf{4.8})$$

where q is the charge carriers (1.60 x 10^{-19}), V is the applied voltage, n is the ideality factor, k is the Boltzmann's constant (1.38 x 10^{-23} J.K^{-1}), T is the temperature taken as 300 K and I_s is the saturation current. The saturation current can be defined as follows [72]:

$$\mathrm{I_s} = \mathrm{A^*ST^2}\exp\left(\frac{q\emptyset_b}{kT}\right) \qquad (\mathbf{4.9})$$

where $A^*$is the Richardson constant, which is 32 A.cm^{-2}K^{-2} for ZnO materials; S is the diode area taken as 0.4 cm^2; and $\emptyset_b$ is the barrier height of the diode. Finally, n is the ideality factor of the photodiode, which was obtained from the slopes of the ln (I) versus V, and is given follows [73]:

$$\mathrm{n} = \frac{\mathrm{q}}{\mathrm{kT}}\frac{\mathrm{dV}}{\mathrm{dln(I)}} \qquad (\mathbf{4.10})$$

The barrier height can be calculated using I-V characteristics under dark conditions using the following equation [67, 73, 74]:

$$\emptyset_\mathrm{b} = \frac{kT}{q}.\ln\left(\frac{\mathrm{AA^*T^2}}{\mathrm{I_s}}\right) \qquad (\mathbf{4.11})$$

As presented in Table 4.7, diode parameters were calculated from the I-V characteristics under illumination and dark conditions. The calculated values of barrier height, saturation current and ideality factor for n-GZO deposited onto a p-Si photodiode structure were compatible with other studies in the literature [72, 75, 76]. In this study, the ideality factor and saturation current decreased depending on the

thickness of GZO thin films, while the barrier height increased with increasing thickness of GZO thin films.

In addition to *n* being an indicator for the ideality behavior of a diode, its value revealed which carrier transport mechanism was dominant in the device. The dominant mechanisms for n interval were the tunneling current, the generation-recombination current and leakage current for $1 < n < 2$, $n = 2$, and $n > 2$, respectively. Accordingly, in this study, the generation-recombination current mechanism was efficient for GZO with the thinnest layer, but the leakage current mechanism was valid for other devices. The ideality factor of the fabricated diodes may have been greater than 1 because of the natural oxide layer, such as SiO_2 on Si, tunneling and series resistance [77, 78].

In addition, the lower GZO thin film resistance can give rise to the relatively large forward biased current and small ideality factor. The high barrier height can restrict a saturation current that results in a high built-in electric field. The existence of interface states supports an increase in saturation current as well. Overall, improvement of these results depends on the thinnest of the device's GZO thickness.

The photosensitivity is the ratio of photocurrent (I_{ph}) to dark current (I_{dark}) at the specific voltage, given in equation (4.12) [79],

$$PS = \frac{I_{ph}}{I_{dark}} \qquad (\mathbf{4.12})$$

The rectification ratio is proportional to the forward current (I_F) and the reverse current (I_R) at the specific voltage in dark condition, given in equation (4.13),

$$RR = \frac{I_F}{I_R} \qquad (\mathbf{4.13})$$

Responsivity (R) of a photodiode, as displayed in equation (4.14), is dependent on photocurrent and input power [79, 80],

$$R = \frac{I_{ph}}{P_{in}\, A} \qquad (\mathbf{4.14})$$

where I_{ph} is photocurrent, P_{in} is input power of solar radiation (100 mW/cm^2) and A is the illuminated area of the diode (1 cm^2).

The photosensivity (PS), rectification ratio (RR) and responsivity (R), are calculated using the I-V graph, are given in Table 4.7. In addition, the I-V graph indicates the devices exhibit the ideal photodiode behavior. Accordingly, the light does not affect the current in the forward bias; only in the reverse bias is it sensitive to light. To the best of our knowledge, photodiode with the thinnest GZO layer, with 35 nm thickness, gives the excellent results for photosensitivity particularly in the reverse bias compared to the literature under different light sources, such as AM1.5 and UV light sources with different wavelengths and powers by obtaining an important PS of 4639, which may the best data published for n-GZO/p-Si heterojunction photodiodes until now (presented in Table 4.8).

If the wavelength of the light is larger than λ_t, which conforms to band gap edge of GZO thin films, light cannot be absorbed into the GZO thin film layer and can pass through the GZO thin film. After this movement through the GZO thin film, light can arrive in the silicon layer. The minority carriers, produced in the thin film layer, must arrive in the depletion region to support the PS. This happens at the intersection between the p and n regions. Then, the minority carriers pass through the electric field in the depletion region in order to distinct free electrons and holes. In the wake of this motion, the minority charge carriers drift to the electrodes. The thinner the GZO film layer, the easier it becomes for the free electrons flow towards the electrodes. The photocurrent of the photodiode devices with a thicker GZO film layer is significantly reduced throughout the illuminated time. A thicker GZO film layer is less likely to gather photocarriers; therefore, the photosensitivity value for photodiode devices with thicker GZO film is significantly low.

The penetration depth is calculated using equation (4.15)

$$d\,(\lambda) = \frac{1}{\alpha(\lambda)} \qquad (\mathbf{4.15})$$

The λ_t was found to be 322 nm, 362 nm and 375 nm for GZO-1, GZO-3 and GZO-5, respectively and d (λ) was calculated as 34.7 nm, 103.15 nm and 172.26 nm for GZO-1, GZO-3, and GZO-5, respectively. Generally, the value of the depletion layer for n-ZnO/p-Si was roughly 0.34 μm [81], which complies with the wavelength of λ_d = 460 nm. The incident light was absorbed by the GZO layer for $\lambda < \lambda_t$, in the depletion region for $\lambda_t < \lambda < \lambda_d$ and out of the depletion region of the Si layer for $\lambda > \lambda_d$. Hence, the photogenerated carriers were generated either in the condition of $\lambda < \lambda_t$ or $\lambda_t < \lambda < \lambda_d$. The AM1.5 light spectrum was selected for $\lambda_t < \lambda < \lambda_d$ in order to see the effect of GZO layer thicknesses on devices in this study.

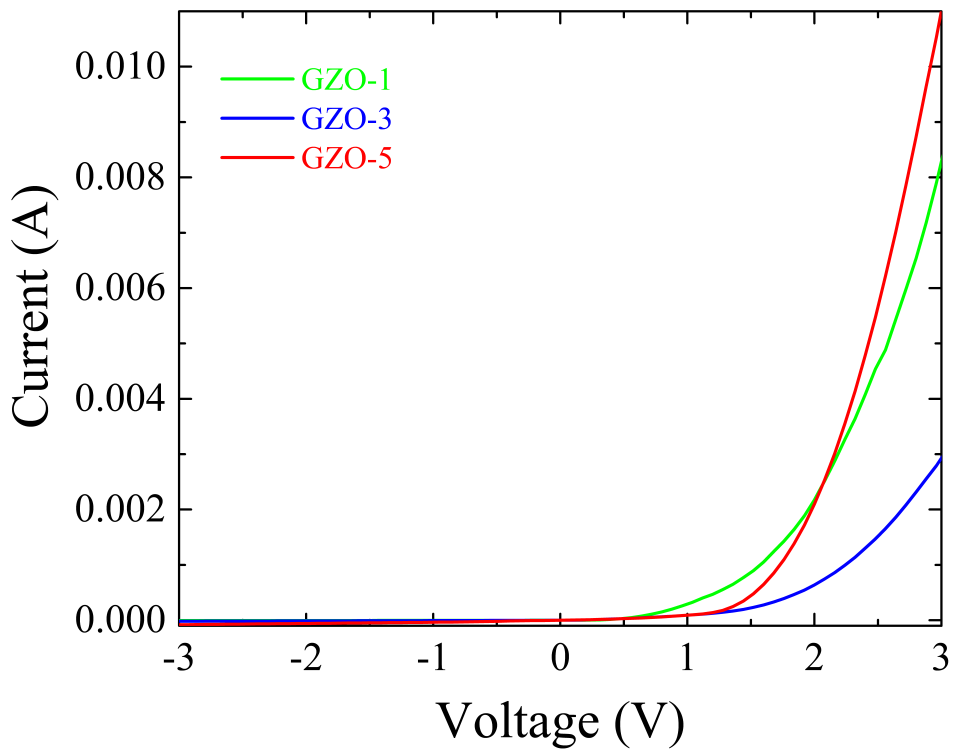


Figure 4.8 Current-voltage curve for n-GZO/p-Si photodiodes under dark conditions

Also, the rectifying behavior investigated in this study was for a n-GZO/p-Si heterojunction photodiode. The RR increased from 144 to 1275 when decreasing the thickness of GZO thin film for n-GZO/p-Si hetero-junction photodiodes.

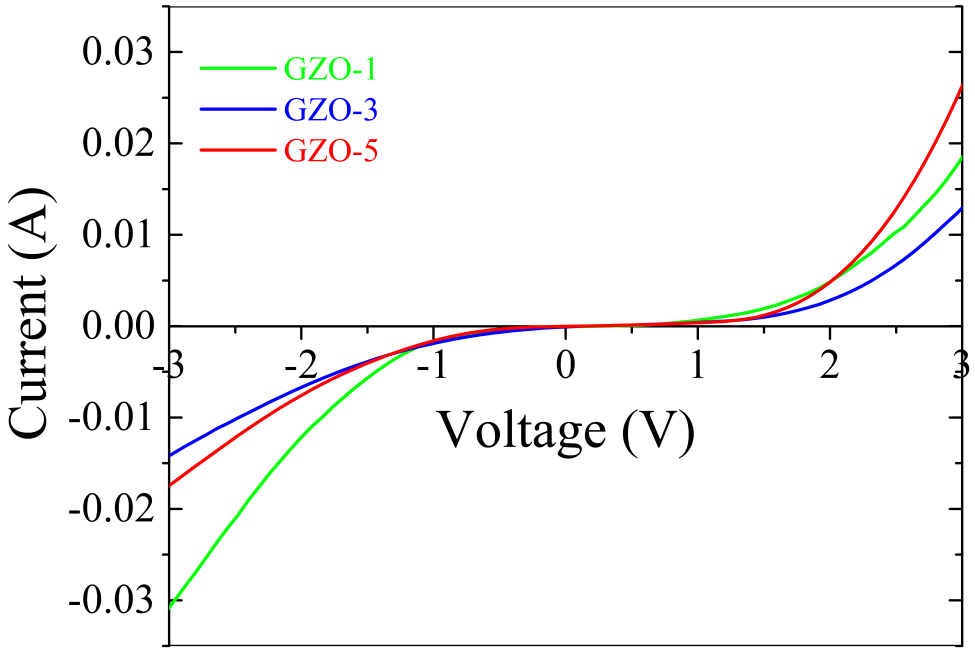


Figure 4.9 Current-voltage curve for GZO/p-Si photodiodes under light condition

Table 4.7 List of I_s, n, $\emptyset_b$ and PS, RR and R

Sample	**I_s (A)**	**n**	**$\emptyset_b$ (V)**	**PS (-3V)**	**RR (±3V)**	**R (A/W) (-3V)**
GZO-1	2.98×10^{-8}	1.98	0.81	4639	1275	0.32
GZO-3	4.12×10^{-7}	2.91	0.76	826	174	0.30
GZO-5	1.43×10^{-6}	4.53	0.72	219	141	0.28

The RR had the best value in the device with the thinnest GZO film layer because saturation current was low for the device with the thinnest GZO film layer, which is attributed to lower of defects in the structure of the film and a low ideality factorResponsivity was diminished from 0.32 to 0.28 when increasing the thickness

of GZO thin films. The parameters of PS, RR and R are listed in Table 4.8 and compared with other studies.

Table 4.8 The comparison of PS, RR and R for ZnO/Si with the previous works

Structure	**Method**	**Light Source**	**PS**	**RR**	**R (A/W)**	**Year**	**Ref.**
GZO/Si	Sol-gel	AM1.5	4639 (-3V)	1275 (±3V)	0.32 (-3V)	2018	This Work
GZO/ZnO/Glass	Hydrothermal	UV	15.2 (-1V)	-	-	2016	[47]
GZO/Si	Sputtering	AM1.5	-	100 (±1V)	-	2016	[48]
GZO/Si	Sol-gel	UV	73.3 (-5V)	-	46.2 (5V)	2017	[45]
BGZO/ZnO/Si	Sputtering	UV	490 (-4V)	2500 (±5V)	-	2018	[20]
ZnO: GO/Si	Sol-gel	AM1.5	1500 (-3V)	-	0.5 (4V)	2015	[82]
AZO/Si	Sol-gel	UV	36.2 (-10V)	578.5 (±20V)	-	2012	[83]
ZnO/Si	Sol-gel	UV	23 (-5V)	5700 (±5V)		2009	[84]
AZO/Si	Sputtering	Halogen	2.29 (-5V)	19.7 (±5V)		2009	[22]
ZnO/Si	Ion-beam	Red laser	48.4 (-5V)	-	0.28 (-5V)	2003	[85]

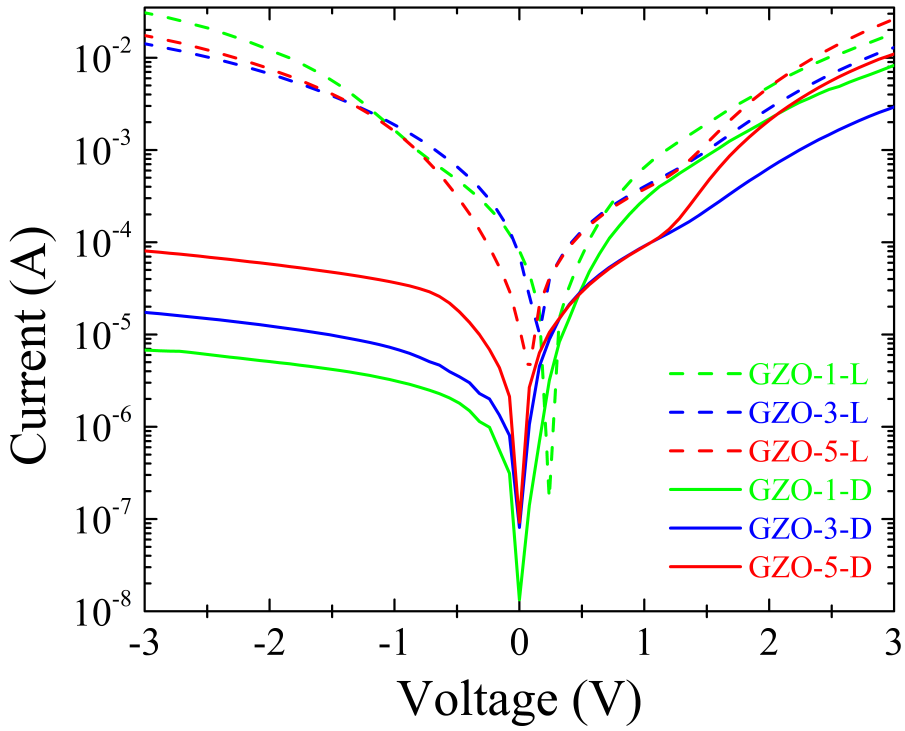


Figure 4.10 The semilog I-V graph with different thicknesses under light and in the dark

CHAPTER 5

CONCLUSION

In this study, Ag/n-GZO/p-Si/Ag heterostructure photodiodes were fabricated with different thicknesses using the sol-gel spin coating method. Each coating cycle roughly corresponded to 35 nm thicknesses. Accordingly, the effect of the thickness of the GZO layer on structural, morphological, optical and electrical performances was investigated using characterization tools.

The XRD results indicated that the average grain size was reduced from about 23 nm to 20 nm due to the increased thickness of GZO thin films, which is significantly diminishes grain boundaries. The TC value was dependent on the RMS value as well. Therefore, all devices have extensions in the lattice of the crystal structure because their strain value was calculated as positive. Consequently, the strain on the Si layer was greatly reduced in devices with the thinner GZO layer.

AFM results provide information about devices' surfaces morphologies. Because the RMS value is small, the devices' surfaces were smooth, which diminished the scattering of light and developed the transmittance of the GZO films.

The SEM measurements were carried out to obtain thickness of GZO thin films on silicon substrates.

The UV-VIS-NIR measurements indicated that high transparency of the films boosts the photoresponse performance of the device. Thus, the best performance was obtained in the thinner layered device with the best transparency and high crystal quality.

Whole devices were measured under AM1.5 illumination and in the dark to obtain I-V characteristics. In this study, all devices behaved as diodes and were particularly sensitive to light applied in the reverse bias region. Not only was the RR is the best

in the device with thinner GZO film, but PS also the best in the device with thinner GZO film. The R had the same trend as the RR and PS.

The diode performance was improved by tuning the thickness of the thin film layer of GZO/p-Si heterojunction since the transparency of the GZO films was high. This tuning made the free charges more easily flow to electrodes. The obtained results clearly reveal that n-GZO/p-Si photodiodes have good properties, in term of structural, morphological and electrical, as a device.

This photodiode device with the thinnest GZO layer (fabricated using low-cost sol-gel method) had the desired sensor properties and photoelectronic applications.

As a result, the device with the thinner GZO layer was an improvement in diode, photodiode. Considering these findings, when the following applied to devices, can produce better devices, such as diodes, photodiodes and solar cells:

- Obtaining a thinner GZO thin film layer on Si structure,
- Changing the ratio of gallium dopant,
- Changing the solution molarity,
- Changing the annealing temperature during the experiment,
- Changing the annealing temperature during the experiment to increase the electrical conductivity of the GZO layer,
- Adding a new interlayer to the ZnO/Si structure to eliminate the negative effects of the interface,
- Using better conductive contacts considering work function of contacts instead of Ag contacts,
- Considering the different orientation and thickness of the silicon substrates are used in the experiment,

- Adding metal nanoparticles of different sizes and shapes, such as gold and silver, to the top layer, interlayer or bottom layer of ZnO to boost performance of device.

REFERENCES

[1] Sharma, S. K., Singh, S. P., & Kim, D.Y. Fabrication of the heterojunction diode from Y-doped ZnO thin films on p-Si substrates by sol-gel method. Solid State Communications, 270 (2018), 124-129, 2018.

[2] Lee, C.-S., Jeon, C.-H., Lee, B.-T., & Jeong, S.-H. Abrupt conversion of the conductivity and band-gap in the sputter grown Ga-doped ZnO films by a change in growth ambient: Effects of oxygen partial pressure. Journal of Alloys and Compounds, 742 (2018), 977-985. 2018.

[3] Yang, J., Jiang, Y., Li, L., & Gao, M. Structural, morphological, optical and electrical properties of Ga-doped ZnO transparent conducting thin films. Applied Surface Science, 421 (2017), 446-452. 2017.

[4] Mitta, S. B., Murahari, P., Nandanapalli, K. R., Mudusu, D., R., Karuppannan, & Whang, D. Si:ZnO heterostructures for efficient diode and water-splitting applications, International Journal of Hydrogen Enegry, 43 (2018), 16015-16023. 2018.

[5] Srinatha, N., Raghu, P., Mahesh, H. M., & Angadi, B. Spin-coated Al-doped ZnO thin films for optical applications: Structural, micro-structural, optical and luminescence studies. Journal of Alloys and Compounds, 722 (2017), 888-895, 2017.

[6] Horng, R.-H., Ou, S.-L., Huang, C.-Y., Ravadgar, P., & Wu, C.-I. Effects of Ga concentration and rapid thermal annealing on the structural, optoelectronic and photoluminescence properties of Ga-doped ZnO thin films. Thin Solid Films, 605(2016), 30-36. 2016.

[7] Pugalenthi, A. S., Balasundaraprabhu, R., Gunasekaran, V., Muthukumarasamy, N., Prasanna, S., & Jayakumar, S. Effect of thickness on the structural, optical and electrical properties of RF magnetron sputtered GZO thin films. Materials Science in Semiconductor Processing, 29 (2015), 176-182. 2015.

[8] Chen S., Warwick, M. E. A., & Binions, R., Effects of film thickness and thermal treatment on the structural and opto-electronic properties of Ga-doped ZnO films deposited by sol–gel method. Solar Energy Materials and Solar Cells, 137 (2015), 202-209. 2015.

[9] Chongsri, K., & Pecharapa, W. UV photodetector based on Al-doped ZnO nanocrystalline sol-gel derived thin fims. Energy Procedia, 56 (2014), 554-559. 2014.

[10] Ding, M., Guo, Z., Zhou, L., Fang, X., Zhang, L., Zeng, L., Xie, L., & Zhao, H., One-Dimensional Zinc Oxide Nanomaterials for Application in High-Performance Advanced Optoelectronic Devices. Crystals, 8 (5), 2018.

[11] Nam, G. M. and Kwon, M. S. Transparent conducting Ga-doped ZnO thin film for flat-panel displays with a sol-gel spin coating. Journal of Information Display, 9 (3), 8-11. 2008.

[12] Kim, T. W., Choo, D. C., No, Y. S., Choi, W. K., & Choi, E. H. High work function of Al-doped zinc-oxide thin films as transparent conductive anodes in organic light-emitting devices. Applied Surface Science, 253 (2006), 1917-1920. 2006.

[13] You, H.-C. & Wang, C.-J. Low-Temperature, Solution-Processed, Transparent Zinc Oxide-Based Thin-Film Transistors for Sensing Various Solvents. Materials, 10 (3). 2017.

[14] Liang, H. K., Yu, S. F., & Yang, H. Y. ZnO random laser diode arrays for stable single-mode operation at high power. Applied Physics Letters, 97, 2010.

[15] Pietruszka, R., Witkowski, B. S., Zielony, E., Gwozdz, K., Placzek-Popko, E., & Godlewski, M. ZnO/Si heterojunction solar cell fabricated by atomic layer deposition and hydrothermal methods. Solar Energy, 155 (2017), 1282-1288. 2017.

[16] Hjiri, M., Mir, L. El, Leonardi, S. G., Pistone, A., Mavilia, L., & Neri, G. Al-doped ZnO for highly sensitive CO gas sensors. Sensors and Actuators B: Chemical, 196 (2014), 413-420. 2014.

[17] Farooq, W. A., & Yakuphanoglu F. Photoresponse and electrical characterization of photodiode based nanofibers ZnO and Si. Materials Science in Semiconductor Processing, 14 (2011), 207-211. 2011.

[18] Hazra, P., Singh, S. K., & Jit, S. Ultraviolet Photodetection Properties of ZnO/Si Heterojunction Diodes Fabricated by ALD Technique Without Using a Buffer Layer. Journal of Semiconductor Technology and Science, 14 (1), pp. 117-123, 2014.

[19] Chen, X.L., Xu, B.H., Xue, J.M., Zhao, Y., Wei, C.C., Sun, J., Y. Wang, Zhang, X.D., & Geng,X.H. Boron-doped zinc oxide thin films for large-area solar cells grown by metal organic chemical vapor deposition. Thin Solid films, 515 (2007), pp. 3753-3759. 2007.

[20] Lu, Y., Huang, J., Li, B., Tang, K., Ma,Y., Cao, M, Wang L., & Wang, L. A boron and gallium co-doped ZnO intermediate layer for ZnO/Si heterojunction diodes. Applied Surface Science, 428 (2018), 61-65. 2018.

[21] Bedia, F. Z., Bedia, A., Benyoucef, B., & Hamzaoui, S. Electrical characterization of n-ZnO/p-Si heterojunction prepared by spray pyrolysis technique. Physics Procedia, 55 (2014), 61-67. 2014.

[22] Bo, H., Quan, M. Z., Jing, X., Lei, Z., Sheng, Z. N., Feng, L., Cheng, S., Ling, S., Yue, Z. C, Shan, Y. Z., & Ting, Y. Y. Characterization of AZO/p-Si heterojunction prepared by DC magnetron sputtering. Materials Science in Semiconductor Processing, 12 (2009), 248-252. 2009.

[23] Nguyen, N. G., Ho, V. T. T., & Hong, L.-S. Low-resistivity, high-transmittance Ga:ZnO films prepared through metalorganic chemical vapor deposition using an inexpensive solution of diethylzinc in n-hexane as the Zn precursor. Applied Physics Letters, 102 (18). 2013.

[24] Kahraman,S., Çakmak, H. M., Çetinkaya, S., Bayansal, F., Çetinkara, H. A., & Güder, H. S. Characteristics of ZnO thin films doped by various elements. Journal of Crystal Growth, 363 (2013), 86-92. 2013.

[25] Ivanova, T., Harizanova, A., Koutzarova, T., Vertruyen, B., & Stefanov, B. Structural and morphological characterization of sol-gel ZnO:Ga films: Effect of annealing temperatures. Thin Solid Films, 646 (2018), 132-142. 2018.

[26] Znaidi, L., Touam, T., Vrel, D, Souded, N., Yahia, S. B., Brinza, O., Fischer A. & Boudrioua, A. AZO Thin Films by Sol-Gel Process for Integrated Optics. Coating, 3 (3), 126-139. 2013.

[27] Tsay, C.-Y., Fan, K.-S., & Lei, C.-M. Synthesis and characterization of sol–gel derived gallium-doped zinc oxide thin films. Journal of Alloys and Compounds, 512 (1), 216-222. 2012.

[28] Chaabouni, F., Khalfallah, B., & Abaab, M. Doping Ga effect on ZnO radio frequency sputtered films from a powder target. Thin Solid Films, 617 (2016), 95-102. 2016.

[29] Hassan, A., Jin,Y., Chao,F., Irfan, M., & Jiang, Y. Dopant-driven enhancements in the optoelectronic properties of laser ablated ZnO: Ga thin films. Journal of Applied Physics, 123 (16). 2018.

[30] Ferdaous, M. T., Shahahmadi, S. A., Sapeli, M. M. I., Chelvanathan, P., Akhtaruzzaman, Md., Tiong, S. K., & Amin, N. Interplay between variable direct current sputtering deposition process parameters and properties of ZnO:Ga thin films. Thin Solid Films, 660 (2018), 538-545. 2018.

[31] Patra, S., Ray, A., Roy, A., Sadhukhan, P., Pujaru, S., Ghorai, U. K., Bhar, R., & Das, S. ZnO polymer composite based visible blind UV photo detector. Materials Research Bulletin, 101 (2018), 240-245. 2018.

[32] Dhahri, R., Hjiri, M., Mir, L. E., Bonavita, A., Iannazzo, D., Leonardi, S.G., & Neri, G. CO sensing properties under UV radiation of Ga-doped ZnO nanopowders. Applied Surface Science, 355(2015), 1321-1326. 2015.

[33] Jäger, K., Isabella, O., Smets, A. H. M., & René A. C. M. M., Swaaij, V., & Zeman, M. Solar Energy Fundamentals,Technology, and Systems. 2014.

[34] Neamen, D. A. Semiconductor Physics and devices. (4th ed.). New York. McGraw-Hill Companies. 2012.

[35] pn junction diode under thermal equilibrium. (n.d.). Retrieved December 26, 2018, from https://en.wikipedia.org/wiki/P–n_junction.

[36] PN Junction Diode. (n.d.). Retrieved October 3, 2018, from https://www.electronics-tutorials.ws/diode/diode_3.html.

[37] p–n junction. (n.d.). Retrieved October 4, 2018, from https://en.wikipedia.org/wiki/P–n_junction.

[38] pn junctin under forward bias and reverse bias. (n.d.). Retrieved December 26, 2018, from http://www.optique-ingenieur.org/en/courses/OPI_ang_M05_C02/co/Contenu_06.html.

[39] Abid, K. Gated Lateral Silicon p-i-n Junction Photodiodes. Unpublished Ph.D thesis, College of Science & Engineering School of Engineering, University of Glasgow. 2011.

[40] Xu, Y. Fabrication and Characterization of Photodiodes for Silicon Nanowire Application and Backside Illumination. Unpublished master' s thesis, Electro-Optics, University of Dayton. 2015.

[41] Photodiode. (n.d.). Retrieved October 10, 2018, from https://en.wikipedia.org/wiki/Photodiode - Photovoltaic_mode.

[42] Haapalinna, A. Characterization Methods for Silicon Photodiode and Silicon Sub-Surface Properties. Unpublished Ph.D thesis, Department of Electrical and Communications Engineering. Helsinki University of Technology. 2004.

[43] HAMAMATSU. Si photodiodes. (n.d.). Retrieved October 18, 2018, from https://www.hamamatsu.com/resources/pdf/ssd/e02_handbook_si_photodiode.pdf.

[44] Photodiode Characteristics and Applications. (n.d.). Retrieved October 18, 2018, from http://www.osioptoelectronics.com/application-notes/an-photodiode-parameters-characteristics.pdf.

[45] Tsay, C.-Y., & Hsu, W.-T., "Comparative Studies on Ultraviolet-Light-Derived Photoresponse Properties of ZnO, AZO, and GZO Transparent Semiconductor Thin Films," Materials, 10 (12), 10804-10808. 2017.

[46] Yang, L., Zhou, H., Xue, M., Song, Z., & Wang, H. A self-powered, visible-blind ultraviolet photodetector based on n-Ga:ZnO nanorods/p-GaN heterojunction. Sensors and Actuators A: Physical, 267 (2017), 76-81. 2017.

[47] Young, S.-J., Chiou, C.-L., Liu, Y.-H., & Ji, L.-W. Synthesis of Ga-Doped ZnO Nanorods by Hydrothermal Method and Their Application to Ultraviolet Photodetector. Inventions, 1(1). 2016.

[48] Akgul, G., Akgul, F. A., Unalan, H. E., & Turan, R. Photovoltaic performance of Gallium-doped ZnO thin film/Si nanowires heterojunction diodes. Philosophical Magazine, 96 (11), pp. 1093-1109. 2016.

[49] Lin, T.-C., Huang, W.-C., Horng, C.-T., & Yang, S.-H. The Electrical Characteristics of ZnO :Ga/p-Si Junction Diode. MRS Proceedings, 1494, 105-110. 2013.

[50] Yang, P. Y., Wang, H., Wang, X. N., Zhang, J., & Jiang, Y. Optical and Electrical Properties of Ga-Doped ZnO Nanorod Arrays Fabricated by Thermal Evaporation. Journal of Nanoscience and Nanotechnology, 11 (12), 10804-10808, 2011.

[51] Cullity, B. D. Elements of X-Ray Diffraction (8th ed.).Addison-Wesley Publishing Company. 1978.

[52] Atomic Force Microscopy (AFM). (n.d.). Retrieved October 18, 2018, from http://users.metu.edu.tr/chem355/assets/11-355-AFM.pdf.

[53] How AFM Works. (n.d.). Retrieved October 17, 2018, from https://www.parksystems.com/index.php/medias/nano-academy/how-afm-works.

[54] Scanning Electron Microscope. (n.d.). Retrieved October 17, 2018, from https://www.microscopemaster.com/scanning-electron-microscope.html.

[55] UV-VIS-NIR spectroscopy: what is it & what does it do?. (n.d.). Retrieved October 18, 2018, from http://www.vam.ac.uk/content/journals/conservation-journal/issue-01/uv-vis-nir-spectrocopy-what-is-it-and-what-does-it-do/.

[56] Habubi, N. F., Mousa, A. O., & Nema, N. A. Fabrication and Characterization of ZnO/p-Si Heterojunction Solar Cell. World Scientific News, 18, 118-132. 2015.

[57] Yildiz, A., Uzun, S., Serin, N., & Serin, T. Influence of grain boundaries on the figure of merit of undoped and Al, In, Sn doped ZnO thin films for photovoltaic applications. Scripta Materialia, 113 (1), 23-26. 2016.

[58] Yildiz, A., Cansizoglu, H., Abdulrahman, R., & Karabacak, T. Effect of grain size and strain on the bandgap of glancing angle deposited AZO nanostructures. Journal of Materials Science: Materials in Electronics, 26 (8), 5952-5957. 2015.

[59] Yildiz, A., Serin, T., Öztürk, E., & Serin, N. Barrier-controlled electron transport in Sn-doped ZnO polycrystalline thin films. Thin Solid Films, 522 (1), 90-94. 2012.

[60] Elfadill, N. G., Hashim,M. R., Chahrour, K. M., Qaeed, M.A., & Bououdina, M. The influence of Cu_2O crystal structure on the Cu_2O/ZnO heterojunction photovoltaic performance. Superlattices and Microstructures, 85 (2015), 908-917. 2015.

[61] Ilican, S., Gorgun, K., Aksoy, S., Caglar, Y., & Caglar, M. Fabrication of p-Si/n-ZnO:Al heterojunction diode and determination of electrical parameters. Journal of Molecular Structure, 1156 (2018), 675-683. 2018.

[62] Kumar, M., Kumar, A. & Abhyankar, A. C. Influence of texture coefficient on surface morphology and sensing properties of W-doped nanocrystalline tin oxide thin films. Applied Materials & Interfaces, 7 (6), 3571–3580. 2015.

[63] Mahdhi, H., Alaya, S., Gauffier, J. L., Djessas, K., & Ayadi, Z. B. Influence of thickness on the structural, optical and electrical properties of Ga-doped ZnO thin films deposited by sputtering magnetron. Journal of Alloys and Compounds, 695 (2017),. 697-703. 2017.

[64] Sbeta, M., Atilgan, A., Atli, A., & Yildiz, A. Influence of the spin acceleration time on the properties of ZnO:Ga thin films deposited by sol–gel method. Journal of Sol-Gel Science and Technology, 86 (2), 513-520, 2018.

[65] Kara, I., Yildiz, A., Yildiz, G., Dogan, B., Serin, N., & Serin, T. Al and X (Sn, Cu, In) co-doped ZnO nanocrystals. Journal of Materials Science: Materials in Electronics, 27 (6), 6179-6182. 2016.

[66] Jeong, I. S., Kim, J. H., & Im, S., Ultraviolet-enhanced photodiode employing n-ZnO/p-Si structure. Applied Physics Letters, 83 (14), 2946-2948. 2003.

[67] Singh, S. K., Hazra, P., & Tripathi S. Performance analysis of RF-sputtered ZnO/Si heterojunction UV photodetectors with high photo-responsivity. Superlattices and Microstructures, 91 (2016), 62-69. 2016.

[68] Tari, O., Aronne, A., Addonizio, M. L., Daliento, S., Fanelli, E., & Pernice, P. Sol–gel synthesis of ZnO transparent and conductive films: A critical approach. Solar Energy Materials and Solar Cells, 105 (2012), 179-186. 2012.

[69] Chabane, L., Zebbar, N., Trari, M., & Kechouane, M. Opto-capacitive study of n-ZnO/p-Si heterojunctions elaborated by reactive sputtering method: Solar cell applications. Thin Solid films, 636 (2017), pp. 419-424. 2017.

[70] Serrao, F. J., Sandeep, K. M., Bhat, S., & Dharmaprakash, S. M. High energy electron irradiation effects on Ga-doped ZnO thin films for optoelectronic space applications. Applied Physics A, 124 (3), 124-224. 2018.

[71] Cheung, S. K., & Cheung, N. W. Extraction of Schottky diode parameters from forward current-voltage characteristics. Appl. Phys. Lett., 49 (2), 85-87, 1986.

[72] Somvanshi, D., & Jit, S. Analysis of Temperature-Dependent Electrical Characteristics of n-ZnO Nanowires (NWs)/p-Si Heterojunction Diodes. IEEE Transactions on Nanotechnology, 13 (1), 62-69. 2014.

[73] Orak, I. The performances photodiode and diode of ZnO thin film by atomic layer deposition technique. Solid State Communications, 247 (2016), 17-22. 2016.

[74] R. Zhu, Zhang, X., Zhao, J., Li, R., & Zhang, W. Influence of illumination intensity on the electrical characteristics and photoresponsivity of the Ag/ZnO Schottky diodes. Journal of Alloys and Compounds, 631 (2015), 125-128. 2015.

[75] Chirakkara, S., & Krupanidhi, S. B. Study of n-ZnO/p-Si (100) thin film heterojunctions by pulsed laser deposition without buffer layer. Thin Solid Films, 520 (18), 5894-5899. 2012.

[76] Ynineb, F., Attaf, N., Aida, M. S., Bougdira, J., Bouznit, Y.,& Rinnert, H. Morphological and optoelectrical study of ZnO:In/p-Si heterojunction prepared by ultrasonic spray pyrolysis. Thin Solid films, 628 (2017), 36-42, 2017.

[77] Yıldırım, M. A., Güzeldir, B., Ateş, A., & Sağlam, M. Temperature dependent current–voltage characteristics of the Zn/ZnO/n-Si/Au–Sb structure with ZnO interface layer grown on n-Si substrate by SILAR method. Microelectronic Engineering, 88 (10), 3075-3079. 2011.

[78] Orak, I., Ejderha, K., & Turut, A. The electrical characterizations and illumination response of Co/N-type GaP junction device. Current Applied Physics, 15 (9), 1054-1061. 2015.

[79] Mahdi, M.A., Hassan, J. J., Ng, S.S., Hassan, Z., & Ahmed, N. M. Synthesis and characterization of single crystal CdS nanosheet for high speed photodetection. Physica E, 44 (2012), 1716-1721. 2012.

[80] Sharma, S., Bayer, B. C., Skakalova, V., Singh, G. & Periasamy, C. Structural, Electrical, and UV Detection Properties of ZnO/Si Heterojunction Diodes. IEEE Transactions on Electron Devices, 63 (5), 1949-1956. 2016.

[81] Hassan, M. A. M., Saleh, A. F., & Mezher, S. J., Energy band diagram of In: ZnO/p-Si structures deposited using chemical spray pyrolysis technique. Applied Nanoscience, 4 (6), 695-701. 2013.

[82] Hendi, A. A. Electrical and photoresponse properties of graphene oxide:ZnO/Si photodiode. Journal of Alloys and Compounds, 647 (2015), 259-264. 2015.

[83] Baydoğan, N., Karacasu, O., & Cimenoglu, H. Effect of annealing temperature on ZnO:Al/p-Si heterojunctions. Thin Solid films, 520 (2012), 5790-5796. 2012.

[84] Mridha, S., Dutta, M., & Basak, D. Photoresponse of n-ZnO/p-Si heterojunction towards ultraviolet/visible lights: thickness dependent behavior. J Mater Sci: Mater Electron, 20 (1) 376-379. 2009.

[85] Park, C. H., Lee, J. Y., Im, S., Kim, T. G. n-ZnO/p-Si photodiodes fabricated using ion-beam induced isolation technique. Nuclear Instruments and Methods in Physics Research B, 206 (2003), 432-435. 2003.

CURRICULUM VITAE



PERSONAL INFORMATION

Name Surname : Nur Efşan Köksal

Date of Birth : 1991

Phone :

E-mail : nekoksal@ybu.edu.tr

EDUCATION

Bachelor : Erciyes University / Kayseri (2009-2014) (3.18/4.00)

Master Degree : Ankara Yıldırım Beyazıt University / Ankara (2016/continued)

WORK EXPERIENCE

Research Assist. : Ankara Yıldırım Beyazıt University (2018-continued)

Niğde Ömer Halisdemir University (2017–2018)

TOPICS OF INTEREST

- Optoelectronic device

PUBLISHED WORK

SCI Publications

2018

1. **Nur Efşan Köksal**, Mohamed Sbeta, Abdullah Yildiz, "GZO/Si photodiodes exhibiting high sensitivity", IEEE Transaction on Electron Devices, 2018, revision.

Conference Proceedings

2018

1. (Oral presentation) **N.E. Koksal**, M. Sbeta, A. Yildiz, 'n-ZnO/p-Si heterostructure as a photodiode', International Congress on the World of Technology and Advanced Materials (WITAM), Kırşehir, September 2018 (full text).

2. (Oral presentation) **N.E. Koksal**, M. Sbeta, A. Yildiz, 'Optimizing of cleaning procedure of Si wafers for photovoltaic applications', International Congress on the World of Technology and Advanced Materials (WITAM), Kırşehir, September 2018 (full text).

3. (Oral presentation) **N.E. Koksal**, M. Sbeta and A. Yildiz,' Effect of GZO Film Thickness on Photosensitivity and PV Property of n-GZO/p-Si Heterojunction Devices', EurasianBioChem, Ankara, April 2018 (abstract).

4. (Oral presentation) M. Sbeta, **N.E. Koksal**, and A. Yildiz,' Dependence of Photoelectric Properties of n-ZnO/p-Si Heterojunction Devices on Thickness of ZnO Films', EurasianBioChem, Ankara, April 2018 (abstract).

5. (Poster) **N.E. Koksal**, M. Sbeta and A. Yildiz,' Influence of precursor concentration on photoelectric properties of n-GZO/p-Si heterojunction devices', EurasianBioChem, Ankara, April 2018 (abstract).

6. (Poster) M. Sbeta, **N.E. Koksal** and A. Yildiz, 'The Effects of Solvent-Stabilizer Combinations on Structural and Optical Properties of Al-Doped ZnO Thin Films Deposited by Sol-Gel Method', EurasianBioChem, Ankara, April 2018 (abstract).

Projects

- BAP-5038, Researcher, “Silikon Bazlı Fotodiyotların Geliştirilmesi için Sarf Malzemesi Alımı”, (2018-2019).
- BAP-5037, Researcher, “Silikon Bazlı Güneş Pillerinin Karakterizasyonu İçin Hizmet Alımı”, (2018-2019).


ANKARA YILDIRIM BEYAZIT ÜNİVERSİTESİ
İSTANBUL